Wave packet dynamics in different electronic states investigated by femtosecond time-resolved four-wave-mixing spectroscopy

7 AUTHORS, INCLUDING:

Arnulf Materny

Jacobs University

198 PUBLICATIONS **2,328** CITATIONS

Wolfgang Kiefer

University of Wuerzburg

878 PUBLICATIONS **9,837** CITATIONS

Wave packet dynamics in different electronic states investigated by femtosecond time-resolved four-wave-mixing spectroscopy

A. Materny, T. Chen, M. Schmitt, T. Siebert, A. Vierheilig, V. Engel, W. Kiefer[*]

Institut für Physikalische Chemie der Universität Würzburg, Am Hubland, 97074 Würzburg, Germany

Abstract. This paper reviews results on wave packet dynamics investigated by means of femtosecond time-resolved four-wave-mixing (FWM) spectroscopy. First, it is shown that by making use of the various degrees of freedom which are offered by this technique information about molecular dynamics on different potential-energy surfaces can be accessed and separated from each other. By varying the timing, polarization, and wavelengths of the laser pulses as well as the wavelength of the detection window for the FWM signal, different dynamics are coherently excited and probed by the nonlinear spectroscopy. As a model system we use iodine in the gas phase. These techniques are then applied to more-complex molecules (gas phase: benzene, toluene, a binary mixture of benzene and toluene; solid state: polymers of diacetylene matrix-isolated in single crystals of monomer molecules). Here, ground-state dynamics are investigated first without any involvement of electronically excited states and then in electronic resonance to an absorption transition in the investigated molecules. Signal modulations result which are due to wave packet motion as well as polarization beats between modes in different molecules. Phase and intensity changes yield information about intramolecular vibrational energy redistribution, population decay (T_1), phase relaxation (T_2), and coherence times.

PACS: 39.90; 33.20.V; 42.65.Dr

Femtosecond time-resolved spectroscopy enables researchers to have a direct view of the ultrafast wave packet dynamics which evolves on molecular potential-energy surfaces (PESs) after coherent excitation [1, 2]. Femtochemistry is one of the most interesting applications since Zewail and coworkers have designed pump–probe experiments to observe chemical reactions in real time (for an overview see [3, 4]). Meanwhile many other fields have been added like investigations of the relaxation dynamics in the liquid phase [5, 6] or ultrafast spectroscopy of semiconductors [7]. In order to understand the elementary processes which take place in molecules after coherent excitation into certain electronic and/or rovibrational states it is advantageous to perform investigations on isolated molecules first [8–11]. On a sub-nanosecond time scale vapour phase or molecular beams offer collision-free conditions. Here, coherently excited wave packets can be observed on a very long time scale without relaxation caused by inter-molecular processes [12–14].

Up to now only a few experiments were performed which directly access the molecular dynamics on the ground-state PES. For bound systems, Baumert et al. reported on the observation of ground-state wave packet dynamics for Na_2 and Na_3 clusters [15, 16]. For strong pump-laser fields, in the Fourier spectrum of the transient Na_2^+ stimulated-emission pumping signal, besides the frequencies belonging to the excited states a feature corresponding to a ground-state vibration could also be observed. Similar experiments were performed for K_2 clusters [17, 18]. A direct observation of ground-state wave packet dynamics is possible by means of transient absorption in the infrared spectral region. This method was applied mainly for the investigation of large molecules [19–21].

A further approach is the so-called NENEPO (NE: negative, NE: neutral, PO: positive) technique, where anions in a molecular beam are coherently excited by femtosecond photo-detachment, resulting in a ground-state wave packet of the neutral molecule. The dynamics are interrogated by femtosecond ionization combined with mass detection. NENEPO was recently applied to investigate the nuclear motion of silver trimers after the negative-to-neutral transition [22]. Vibrationally excited wave packets were also generated by the application of femtosecond stimulated-Raman spectroscopy. By the pump–dump process wave packets were prepared in the electronic ground state of K_2 clusters with mean vibrational quantum numbers $\bar{v} = 6$ and $\bar{v} = 11$ [23].

Leonhardt et al. [24] were the first who applied coherent anti-Stokes Raman scattering (CARS) with a time resolution in the femtosecond range. Since then several groups have reported sub-picosecond and femtosecond time-resolved

[*]Corresponding author.

four-wave-mixing (FWM) experiments [6, 14, 25–33]. Coherent techniques with high time-resolution have been widely employed in condensed-phase studies of vibrational dephasing [6, 24, 28, 34–42]. However, only recently Hayden and Chandler [33] performed femtosecond time-resolved coherent Raman experiments to excite and monitor the evolution of vibrational coherence in gas-phase samples of benzene as well as 1,3,5-hexatriene. Zewail and coworkers [43] used degenerate FWM (DFWM) to replace the probe pulse in a pump–probe scheme. Through this, they were able to increase the selectivity of the probing of the wave packet motion.

In the present paper we review our recent work on femtosecond time-resolved FWM spectroscopy [44–56]. We would like to point out the main advantages of this technique and to emphasize its capability for investigating ground-state dynamics. Very recently, we have demonstrated that by the CARS method one can observe the dynamics of a wave packet either evolving on the ground- or an excited-state PES [44]. The dynamics which shows itself in the CARS transient depends on the relative timing of the three laser pulses giving rise to the nonlinear FWM process. Next to the timing of the laser pulses there are other degrees of freedom which can be varied in order to gain even more information on the ultrafast ro-vibrational dynamics evolving in the excited molecules. The following points will be discussed below: (i) the timing of the laser pulses, as mentioned above; (ii) the polarizations of the laser pulses which enable one to suppress the contributions of the rotational motion of the molecules to the FWM signal; (iii) the laser wavelengths which determine the electronic as well as ro-vibrational resonances and through this the preparation of the wave packets on the PES of the molecules and which also determine which FWM process takes place (CARS, DFWM, or CSRS, which is the Stokes analogue to CARS – coherent Stokes Raman scattering); (iv) the wavelength window which is opened for the detection of the FWM signal and which selects different dynamical information contained in the transients. We will mainly discuss experimental details of our work. Theoretical simulations by means of quantum calculations were also performed [46, 47, 49, 53] and are discussed by Meyer and Engel in this special issue [57].

The paper is organized as follows: in Sect. 1 we introduce the general methodology of the femtosecond time-resolved FWM spectroscopy. A brief description of the experimental set-up is given in Sect. 2. In Sect. 3 we present experimental results and discuss the influence of the different degrees of freedoms mentioned above. Finally, Sect. 4 gives a short summary of this paper.

1 Methodology

In the following, we describe the basic idea of the femtosecond time-resolved FWM experiment. In Fig. 1a, the three different FWM techniques are displayed which were used in our work. CARS, DFWM, and CSRS differ in their laser as well as signal wavelengths. In our experiments we have applied two colours for the lasers in CARS and CSRS spectroscopy. For CARS, the anti-Stokes signal at ν_{aS} is generated by the interaction of two pump-laser pulses at ν_{pu} and
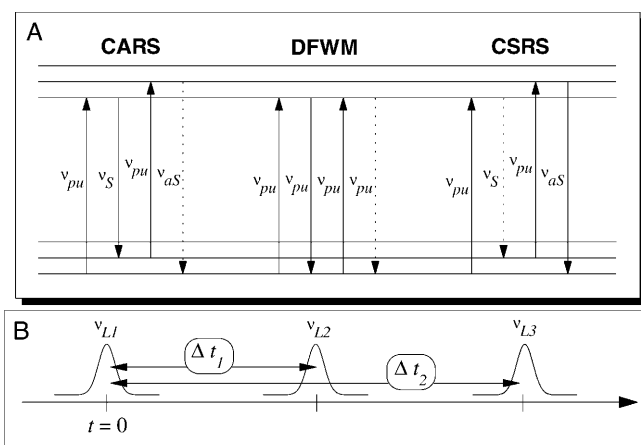
Fig. 1a,b. The FWM processes discussed in this paper. **a** shows representative energy-level diagrams of CARS, DFWM, and CSRS. The signal is depicted by the *dotted lines* in each case. The timing of the laser pulses (where L_1, L_2, and L_3 stand for pu, pu_τ, S, or aS as indicated in **a** can be seen from **b**). Δt_1 and Δt_2 can also take negative values

the Stokes-laser pulse at ν_S with the molecular system. Due to energy conservation $\nu_{aS} = 2\nu_{pu} - \nu_S$ has to be fulfilled. The CSRS signal at ν_S is caused by two pump lasers at ν_{pu} together with a pulse at an anti-Stokes frequency ν_{aS} relative to the pump lasers. Here, $\nu_S = 2\nu_{pu} - \nu_{aS}$ must hold. In the DFWM process all lasers and the signal have the same frequency ν_{pu} and the energy conservation is obeyed by $\nu_{pu} = 2\nu_{pu} - \nu_{pu}$. The schematic representation of the FWM processes in Fig. 1a only shows some of the possible scenarios without a certain time-ordering of the pulses. In Sect. 3, we will discuss more arrangements of the different laser transitions.

As three laser pulses are involved in the FWM process, two delay times can be introduced, separating the pulses from each other. In the experiments presented here, the signal is integrated over time (not delay time). One of the laser pulses defines an arbitrary zero point (see Fig. 1b). The delay times Δt_1 and Δt_2 can be varied in the experiment and positive as well as negative values are possible. In most experiments two of the pulses were chosen to be coincident in time, defining time zero for the transients. Both the coherent excitation and probing of the molecular dynamics are determined by the many degrees of freedom the time-resolved FWM process offers. Of major importance are the timing of the laser pulses and their wavelengths. On the one hand CARS, DFWM, and CSRS access different dynamics and on the other hand each of the processes can make use of resonances with certain molecular states. One distinguishes between electronic and Raman resonances. In the first case, the laser pulses are in resonance with an electronic transition within the molecules. In the second case two laser frequencies are chosen in such a way as to resonantly excite ro-vibrational states in the electronic ground state. The latter is possible without any electronic resonance, which makes FWM an interesting method for the investigation of ground-state dynamics in molecules where no information about the excited-state PES is available. Due to the fact that the ultrashort femtosecond pulses are spectrally broad, in most cases several molecular states are coherently excited, resulting in wave packet excitation and probing.

Due to the phase-matching conditions which have to be fulfilled, the k vectors of the lasers and the signal must not be arranged arbitrarily. Several geometries are possible. In order to suppress stray laser light and also to selectively detect the desired FWM transient in our experiments, a folded BOX-CARS configuration was chosen [58]. Here, the lasers and the signal are well separated and two-beam FWM contributions (e.g. one pump laser interacts twice) can be ruled out due to the direction of their signal k vectors (see Fig. 2).

2 Experimental

In all but one of the experiments discussed in this paper, a 1 kHz Ti:sapphire femtosecond laser system was used. A schematic of the experimental set-up is shown in Fig. 3. Femtosecond pulses of a duration of about 100 fs are generated in a 83 MHz mode-locked Ti:sapphire oscillator (Coherent MIRA), pumped by the multiline output of an Ar^{+}-ion laser (Coherent Innova 310). The pulses have an energy of about 10 nJ and are centred at a wavelength of about 800 nm. Before amplification the pulses are stretched to a duration of about 200 ps. As amplifier we use a regenerative Ti:sapphire system (Clark-MXR) pumped by a frequency-doubled Nd:YAG laser at a repetition rate of 1 kHz. After recompression, the pulses have energies of about 1 mJ and are less than 100 fs long.

In order to have two different colours available, the 800 nm pulse train is divided into two parts by means of a 1:1 beam splitter. Using two four-path OPAs (optical parametric amplifiers, Light Conversion) two independent wavelengths can be chosen. The laser pulses for the experiment were produced using sum frequency generation between signal and idler output of the OPA as well as second-harmonic generation of either the signal or the idler light. To achieve pulse lengths down to about 70 fs, the laser pulses are compressed in double-pass two-prism arrangements.

For the solid-state experiment on polydiacetylenes (PDAs), the laser system (not shown in Fig. 3) consisted of a Ti:sapphire oscillator (Coherent MIRA) and a regenerative amplifier (Coherent RegA 9000) pumping two white-light OPAs (Coherent Model 9400). At the output of the regenerative amplifier the pulses at 800 nm have a repetition rate of 100 kHz. The white-light OPAs generate $\approx$ 100 femtosecond pulses in

Fig. 3. Experimental set-up showing the femtosecond laser system and the beam path of the time-resolved BOXCARS arrangement. Computer-controlled actuators are used to vary the relative arrival time of the femtosecond pulses at the sample. The monochromator is equipped with both photomultiplier tube (PMT) and CCD camera

the range 480–700 nm, with an energy per pulse of approximately 100 nJ.

In all experiments, one of the OPA outputs is branched by a 1:1 beam splitter to produce two of the laser pulses at the same wavelength. The output of the second OPA is used as a third laser pulse. All three beams are aligned parallel to one another and spatially overlapped at the common focus in the sample by the achromatic lens L1. This folded BOX-CARS configuration allows the separation of signal from the incoming laser beams (see discussion above).

The laser pulses can be delayed in time relative to each other by means of Michelson-interferometer arrangements. The FWM transient is recorded as a function of delay time Δt_1 or Δt_2. The relative timing between the different pulses is varied with a computer-controlled actuator that allows optical delays up to 3 ns with a minimal step size of 6 fs. The determination of the position of temporal overlap (time zero) between the different beam pairs is made by using a cross-correlation set-up with second-harmonic generation as well as sum frequency mixing in a thin phase-matched BBO crystal.

The femtosecond FWM signal pulse generated in the sample travels in a direction determined by the phase-matching condition. As this direction is different from that of the incident laser beams, the signal can be separated by a spatial filter. The FWM beam is collimated by a second achromatic lens L2. In order to remove stray laser light and to spectrally analyse the signal, a monochromator (Acton SpectraPro-500) is used. The detection is performed in two ways: (i) a fast photomultiplier tube (RCA C31024 A) measures the light leaving the monochromator. The signal-to-noise ratio in this case is enhanced by means of a boxcar integrator (EG&G model 4121B) in gated-integrator mode, as well as by numerical averaging of several pulses. The latter is also used to smooth the multichannel output of (ii) a CCD camera (Photometrics) which is attached to the monochromator without exit slit. The broadband detection offers many advantages as the

Fig. 2. Scheme of the folded BOXCARS arrangement. L_1, L_2, and L_3 are the three different laser pulses which generate the nonlinear FWM signal

whole spectral range of the FWM signal can be resolved for each pulse [54].

In this paper, we present results on femtosecond investigations of iodine, toluene, benzene, and toluene/benzene mixtures in the gas phase as well as polymers of diacetylenes embedded in diacetylene single crystals. The gas-phase samples were all kept in quartz cells and heated to $\approx 80\,°C$ in order to increase the vapour pressure. For this temperature, the vapour pressure of iodine was $\approx 2\,kPa$, that of benzene $\approx 100\,kPa$, and that of toluene $\approx 50\,kPa$. Therefore, the ratio of the gaseous mixture of benzene and toluene was about 2:1 [59].

The PDA under consideration is FBS (2,4-hexa-diynylene-di-p-fluoro-benzene sulfonate) [60, 61]. FBS was prepared by the method described by Wegner [60]. The single crystals were obtained from solution and had less than 1% contents of polymer. The lozenge-shaped monomer crystals were slightly red-coloured due to the polymer chains which were formed by solid-state polymerization perfectly aligned parallel to the crystal b axis. Therefore, in the visible spectral range one observes a strong dichroic behaviour [62, 63]. The crystals were cleaved parallel to the 100 surface (containing b and c axes) to produce thin platelets of about 100 μm thickness and about 3 mm length in the chain direction ($\parallel b$ axis). For the experiments, the crystals were cooled down in a closed-cycle helium cryostat to a temperature of approximately 8 K.

3 Results and discussion

Here, we demonstrate the main advantages of femtosecond time-resolved FWM spectroscopy by discussing some of our experimental results on different molecules. In most cases iodine served as 'model molecule' and all the new techniques were first applied to this system. However, our goal is to develop a technique which allows the investigation of the wave packet dynamics of more-complex systems. Therefore, we also present some work performed on larger molecules, first in the gas phase (benzene, toluene) and then in the solid state (PDAs).

Since three laser pulses are responsible for the generation of the FWM signal, many degrees of freedom can be varied.

In the following, we first discuss the results obtained from changing the timing of the laser pulses. As an example we use iodine as molecular system and femtosecond CARS as time-resolved FWM method.

3.1 The timing of the laser pulses

In the following, we discuss experiments where three laser fields interact with the ensemble of I_2 molecules in a folded BOXCARS arrangement as mentioned above. First we consider the case where two of these laser pulses are coincident in time, while the third pulse arrives with a variable delay time Δt. Depending on the relative timing of the three laser pulses, different dynamics in the molecules are probed by one- or two-photon interactions resulting in the coherent CARS signal.

In the femtosecond CARS experiment, two laser pulses (pu and pu_τ) have the same wavelength, $\lambda_{pu} = \lambda_{pu_\tau}$. The third laser pulse (S) is tuned to a longer wavelength λ_S in such a way that the difference between pu and S laser wavelengths is resonant with a vibrational Raman transition in the iodine molecule. While one of the pump pulses (pu) and the Stokes pulse S are coincident in time, the second pump pulse pu_τ arrives with a variable delay time. Figure 4 shows the observed CARS intensity as a function of delay time Δt between the pump pulse pu_τ and the two time-coincident pulses pu and S for I_2 vapour. The transient was obtained for a pump wavelength $\lambda_{pu} = \lambda_{pu_\tau} = 559\,nm$ and a Stokes wavelength $\lambda_S = 579\,nm$ detecting the coherent anti-Stokes signal at $\lambda_{aS} = 539\,nm$. For negative delay times ($\Delta t < 0$) of pu_τ, the transient is characterized by beats with a period of approximately 380 fs, which corresponds to an energy difference of $88\,cm^{-1}$. This value agrees with the energy spacing found between the vibrational eigenstates of iodine in the excited B state, which are reached by the $\lambda_{pu_\tau} = 559\,nm$ laser pulse from the ground state. For positive delay times ($\Delta t > 0$) the signal shows oscillations at about twice the frequency of the oscillations at negative delay times ($\Delta t < 0$). These short-time oscillations for $\Delta t > 0$ show a period of 160 fs, corresponding to the wave packet motion prepared by coherent two-photon pumping (pu and S) around the third vibrational
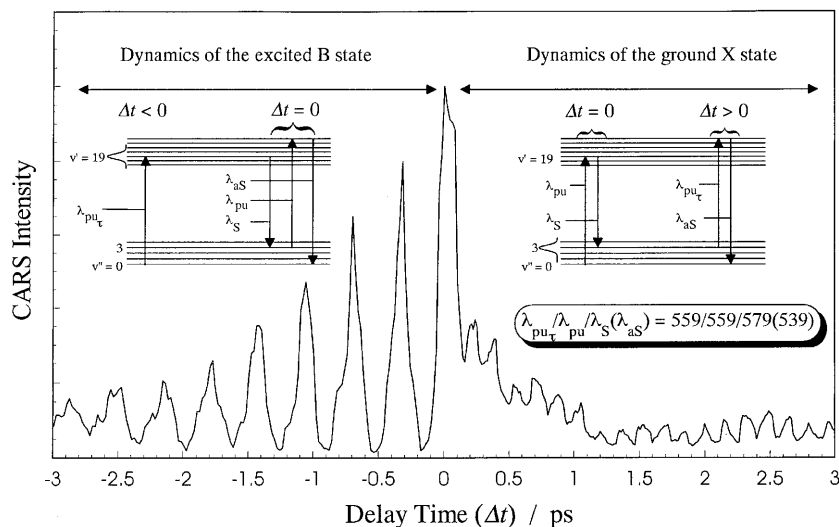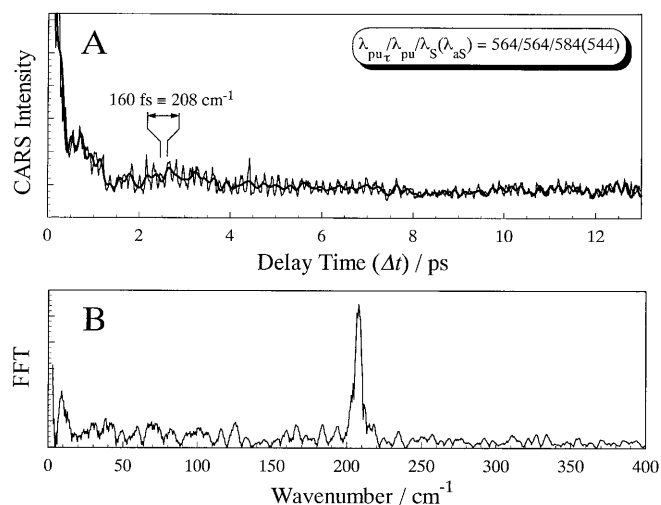

Fig. 4. Iodine femtosecond CARS transient obtained for pump wavelengths $\lambda_{pu} = \lambda_{pu_\tau} = 559\,nm$ and a Stokes wavelength $\lambda_S = 579\,nm$ detecting the CARS signal at $\lambda_{aS} = 539\,nm$. For negative delay times ($\Delta t < 0$), the wave packet dynamics in the excited B state of iodine can be resolved. For positive delay times ($\Delta t > 0$) the transient reflects the motion of the wave packet on the ground X state. Representative energy-level diagrams of the CARS process for both cases $\Delta t > 0$ and $\Delta t < 0$ are shown as *inserts*, indicating the relative timing of the laser pulses

level in the ground X state of iodine, because the wavelength difference between pu and S lasers was tuned to the second overtone ($\Delta v'' = 3$) of the I_2 ground-state vibration. The average period of the oscillations corresponds to a vibrational wavenumber spacing of about $208\ cm^{-1}$. This agrees with the vibrational energy spacing in the ground X state of iodine around $v'' = 3$ as observed from continuum-resonance Raman experiments [64].

In a simplified picture, this can be explained as follows. In the case that pu_τ comes before the time-coincident pulses pu and S, the CARS signal reveals the evolution of the vibrational and rotational coherence of the excited B-state wave functions. Here, the first pulse (pu_τ) creates a wave packet in the excited B state. After a variable time delay ($\Delta t < 0$) this

wave packet is probed by the coherent interaction with the pu and S pulses giving rise to the CARS (aS) signal.

If on the other hand the pump pulse (pu_τ) arrives later ($\Delta t > 0$) than the other two pulses (pu and S), the CARS signal reflects the dynamics in the electronic ground state. In this case the two time-coincident laser pulses (pu and S) prepare a wave packet in the electronic ground state which is probed by the time-delayed third laser pulse (pu_τ), observing the CARS.

In Figs. 5a and 6a, we show CARS transients obtained for iodine taken over longer delay times. Figure 5a gives the long-time behaviour for negative ($\Delta t < 0$) and Fig. 6a that for positive ($\Delta t > 0$) delay times. The peak for $\Delta t = 0$ is not considerably higher than one would expect from the decay behaviour of the oscillations of the excited state. This means that the so-called coherent artifact which was discussed e.g. in [65] plays a minor role in our experiment and resonant contributions dominate the CARS transients of iodine.

In order to analyse the experimental data shown in Figs. 5a and 6a, we give the results of a fast Fourier transform (FFT) of the transients in the corresponding Figs. 5b and 6b. In both FFT spectra, peaks at low wavenumbers (about $5\ cm^{-1}$ for the excited- and $10\ cm^{-1}$ for the ground-state transient in Figs. 5b and 6b, respectively), appear. We assign these features to the rotational dynamics of the molecules. In order to demonstrate the effect of these low-frequency contributions on the transient shape, we removed all components at higher wavenumbers from the FFT spectra and performed a transform back to the time domain. The results are shown in Figs. 5a and 6a (thick lines) for the excited- and ground-state transients, respectively. Figure 7 shows the transients after subtraction of the low-frequency contributions (Fig. 7a: excited state, Fig. 7b: ground state). It is obvious that the slow modulation of the transients at early times (as to be expected) is determined by the low-frequency part of the FFT spectra.

The general shape of the transients is determined by the quantum coherence of vibrations and rotations of the molecules excited. The influence of these coherences on the

Fig. 5. a Femtosecond time-resolved CARS transient showing the wave packet dynamics in the excited B state of iodine ($\lambda_{pu} = \lambda_{pu_\tau} = 551$ nm, $\lambda_S = 570$ nm, $\lambda_{aS} = 528$ nm) and **b** the result of an FFT of this transient. The *insert* shows the band due to transitions $v' \leftarrow v'' = 0$ and $v' + 1 \leftarrow v'' = 0$ in detail. The *thick line* shown in **a** is the low-frequency contribution to this transient obtained from FFT calculations

Fig. 6. a Femtosecond time-resolved CARS transient showing the wave packet dynamics in the ground X state of iodine ($\lambda_{pu} = \lambda_{pu_\tau} = 564$ nm, $\lambda_S = 584$ nm, $\lambda_{aS} = 544$ nm) and **b** the result of an FFT of this transient. The *thick line* shown in **a** is the low-frequency contribution to this transient obtained from FFT calculations

Fig. 7. a Result of a subtraction of the low-frequency contribution from the excited-state transient, both shown in Fig. 5a. **b** Same for the ground-state transient shown in Fig. 6a. The resulting transients show the vibrational coherences of the two different electronic states
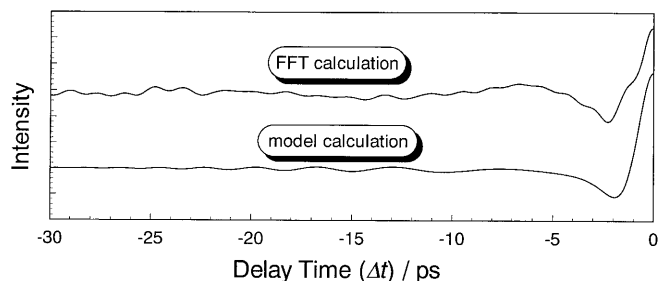
Fig. 8. The *upper curve* shows the low-frequency contribution to the excited-state transient taken from iodine which is also shown in Fig. 5a. It was obtained from FFT calculations (compare Fig. 7a). The *lower curve* is the purely rotational coherence as calculated from the simple model described in the text

shape of the time-dependent signal has been discussed in a number of articles [66–72]. Assuming that the excitation starts from a single ro-vibrational level of the electronic ground state characterized by the quantum numbers (v'', J''), in a simple picture one has to consider the following final states in the electronic excited state: (v_i, J_i') and (v_j, J_j') where due to the $\Delta J = \pm 1$ selection rules $J' = J'' \pm 1$. Furthermore, we assume $v_j' \neq v_i'$. After some calculation one finds two contributions to the transient intensity [72]: (i) a vibrational part

$$I_V(t) \propto \sum_{i,j} A_{Vij} \cos\left(2\pi c [E(v_i') - E(v_j')]\Delta t\right) \tag{1}$$

and (ii) a rotational part

$$I_R(t) \propto \frac{J(J+1)}{2J+1} \cos\left(2\pi c [E(J''+1) - E(J''-1)]\Delta t\right). \tag{2}$$

In order to include more states a summation over all accessed J and v has to be performed weighted by a Boltzmann factor as well as the spectral shape of the laser pulse. If for the polarization of the pump and probe pulses magic-angle conditions [73] are fulfilled (see also Sect. 3.2), no contribution due to rotational anisotropy (2) can be detected. However, the lasers in our experiment were all polarized parallel to each other, resulting in transient shapes determined by both vibrational and rotational coherences.

Using the simple model for the rotational coherence, we are able to simulate the decay behaviour seen for short delay times as well as the rotational recurrences for the excited-state dynamics. The rotational recurrences appear after delay times ($> 500\,\mathrm{ps}$) which are not accessed in our experiments. Figure 8 shows a comparison between the calculated low-frequency contributions of the experimental transient (upper curve) given in Fig. 5a and the simulated short-time behaviour (lower curve) for the excited-state dynamics. Having in mind the rather crude approximations made for the calculations, the theoretical curve fits the shape of the FFT result fairly well. However, we were not able to simulate the contributions of rotational coherence seen for the ground state using this simple approximation. A reason for this is that the model applied does not consider the influence of the Franck–Condon factors, which plays an important role for the calculation of the 'pump–dump' process responsible for the preparation of

the ground-state wave packet. Quantum calculations confirm the simple model discussed above and result in a better reproduction of the ground-state transient [46].

Besides the purely rotational coherence effects, the CARS transients also show the average vibrational frequencies as well as beat patterns due to both the local anharmonicity constants and the rotational–vibrational coupling. The excited-state signal (Fig. 5a) shows oscillations with a period of about 410 fs, corresponding to a vibrational wavenumber spacing of about $81\,\mathrm{cm}^{-1}$. This value agrees with the experimental vibrational energy spacings (vapour phase) in the B state around $v' = 24$ [74,75], which is reached by the $\lambda_{pu} = 551\,\mathrm{nm}$ laser pulse from the ground state. The Fourier spectrum of the CARS transient in Fig. 5a shown in Fig. 5b is consistent with this analysis. Closer inspection of the transform reveals several peaks, corresponding to different vibrational levels excited. Due to a coherent excitation of vibrational energy levels with $\Delta v' = 1, 2$, we find in the Fourier spectrum components at about 80 and $160\,\mathrm{cm}^{-1}$, respectively. The insert in Fig. 5b shows the wavenumber differences of transitions $v' \leftarrow v'' = 0$ and $v' + 1 \leftarrow v'' = 0$ in detail. The resolved components agree well with the wavenumber positions of the lines observed in frequency-domain experiments [74,75].

For the CARS experiment we have chosen a wavenumber difference between pump and Stokes lasers corresponding to the second overtone of the I_2 ground-state vibration. The FFT spectrum of the ground-state CARS transient shown in Fig. 4b reveals a band at about $208\,\mathrm{cm}^{-1}$. Comparing this wavenumber position to wavenumber differences calculated on the basis of RKR values of the electronic ground state taken from [76] shows that the electronic ground state is prepared around $v'' = 3$. That is exactly what could be expected from the experimental conditions as mentioned above.

The modulation of the envelopes of the vibrational transients (compare Fig. 7) is mainly determined by the anharmonicity of the PES. This results in a clearly different appearance of the ground- and excited-state transients. The excited B state of iodine is very anharmonic in the range of the vibrational levels accessed. Therefore, the measured oscillations of the wave packet prepared in the excited B state show clear dephasing and rephasing patterns (Fig. 7a). However, the ground-state wave packet is prepared around $v'' = 3$ where the shape of the PES is close to harmonic. Therefore, the amplitudes of the oscillations seen probing the ground-state dynamics do show much less modulation due to dephasing and rephasing on the considered time scale (Fig. 7b).

Additionally, the damping of the amplitudes due to rotational–vibrational interaction results in vanishing signal intensities after about 40 ps for the excited state (Fig. 7a). On the other hand, the amplitudes of the vibrational modulation seen for the ground-state transient do decrease more slowly (Fig. 7b). While the coupling constants α_e are about the same for the excited B state [77] and the ground state [75], considerably higher vibrational levels are involved in the excited-state dynamics. Therefore, the damping due to the shifts of the vibrational energies caused by the coupling to the rotations of the molecules is more pronounced in the excited- than in the ground-state transients.
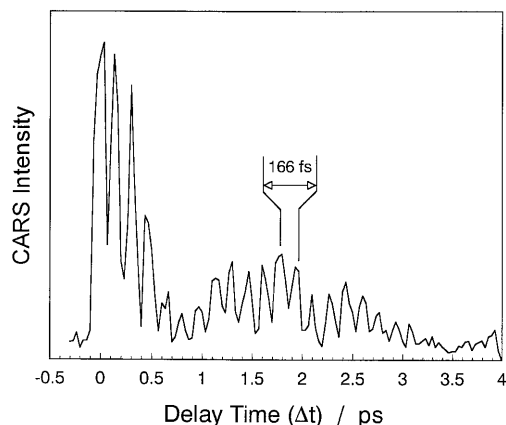
Besides the bands at 80 and $160\,\mathrm{cm}^{-1}$ the FFT spectrum of the excited-state transient (Fig. 5b) shows a band at about $295\,\mathrm{cm}^{-1}$. This wavenumber is about the sum of

the 80 cm^{-1} vibrational spacing in the excited B state and the 208 cm^{-1} belonging to the ground-state vibrational coherence. A possible explanation is the coherent coupling between the electronic ground and excited states due to strong laser interaction [15].

As three laser pulses are interacting with the molecular system, one more delay time can be varied. Up to now we have only considered the case where the delay time between pu and S was set to zero. In order to perform an optimal preparation of a wave packet in the electronic ground state on even higher vibrational states this second time delay can be used.

A selective population of ro-vibronic states of the electronic ground state of alkali dimers was performed more than a decade ago by means of the STIRAP (stimulated Raman process by adiabatic passage) technique [78, 79]. By STIRAP it is possible to perform a complete population transfer from an initial ro-vibronic into a final ro-vibronic state. In the two-colour pump–dump process a first nanosecond laser pulse couples an intermediate and the final state. A time-delayed nanosecond laser pulse subsequently pumps the transition from the initial to the intermediate state. As the interaction times of the laser pulses are much longer than the vibrational and rotational periods, a dressed-state model can be applied for the explanation of the STIRAP process. In the case of femtosecond laser pulses, a different picture must be used. Here, the coherent superposition of several eigenstates form wave packets, which move on the PES of the molecules. Recently, Pausch et al. [23] demonstrated the selective generation and control of excited vibrational wave packets in the electronic ground state of potassium dimers. In the pump–dump experiment wave packets were excited with mean quantum numbers $\bar{v} = 6$ and $\bar{v} = 11$. This stimulated Raman process became effective by first preparing a wave packet on the excited electronic state (resonance condition) and then waiting until the optimal Franck–Condon overlap between the electronic excited state and the target state in the electronic ground state was reached (time delay between pump and dump).

The second time delay in the FWM process enables one to make use of exactly the same effect. In Fig. 9 a CARS transient is shown for iodine, where we have chosen the difference between pump and Stokes laser wavelengths in order to prepare a wave packet in the electronic ground state with mean quantum number $\bar{v} = 10$. The time delay Δt_2 between pu and S (in the experiments presented before, $\Delta t_2 = 0$ was chosen) was adjusted. As soon as the optimum Franck–Condon overlap was reached ($\Delta t_2 \approx 140$ fs) an intense ground-state transient ($\Delta t_1 > 0$, where time zero is defined by the Stokes-laser pulse) could be measured even for this high vibrational state (compare Figs. 4 and 9). Similar experiments were also performed by other groups very recently [80, 81].

3.2 The polarization of the light fields

As was discussed in Sect. 3.1, the CARS transients are determined by the vibrational as well as rotational coherences. The rotational dynamics could be separated from the vibrational by means of applying a theoretical model to the experimental data. In addition to the selectivity that can be achieved by the timing of the lasers (see above), a further discrimination between isotropic and anisotropic contributions to the FWM signal can be attained with specific polarization geometries
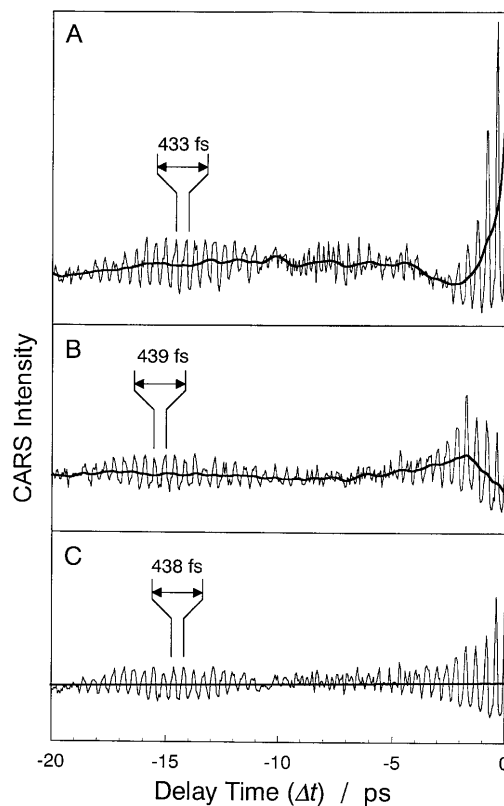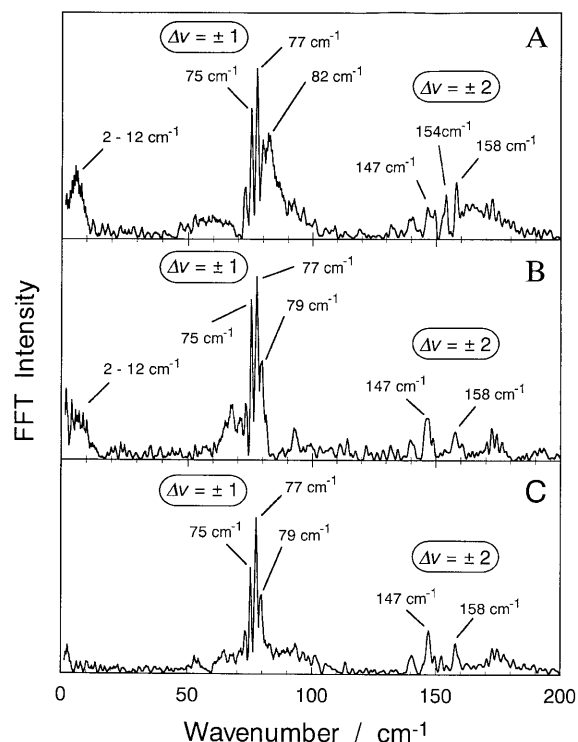

Fig. 10a–c. Femtosecond CARS transients for negative delay times ($\Delta t < 0$) recorded under different polarization geometries ($\lambda_{pu_\tau} = \lambda_{pu} = 541$ nm; $\lambda_S = 560$ nm; $\lambda_{aS} = 529$ nm). The two simultaneous laser pulses pu and S were polarized in a parallel orientation to one another. The polarization of the time-variable laser pulse pu_τ was oriented relative to the simultaneous laser pulses at an angle of $0°$, $90°$ and $54.7°$ for the **a** parallel, **b** perpendicular, and **c** magic-angle polarization geometry, respectively. The *thick lines* show the rotational coherences obtained under the different polarization geometries (for details see text)

Fig. 9. Femtosecond CARS transient taken from iodine ($\lambda_{pu} = \lambda_{pu_\tau} = 550$ nm, $\lambda_S = 625$ nm, $\lambda_{aS} = 491$ nm). The ground-state transient is shown as a function of delay time Δt_1 (> 0) between pu_τ and S. The delay time Δt_2 between pu and S was chosen to be 140 fs (pu first). The oscillations have a period of approximately 166 fs which is in accordance with the wavenumber difference of the vibrational states around $v \approx 10$

of the three laser fields interacting with the molecules. This in turn allows for the separation of the rotational from the vibrational dynamics in the various electronic states of the molecular system [72, 73, 82, 83]. Figure 10 shows three femtosecond CARS transients recorded with a parallel (Fig. 10a), perpendicular (Fig. 10b), and a magic-angle (Fig. 10c) polarization geometry for negative delay times ($\Delta t < 0$) of the time-variable laser pulse pu_τ.

The intensity of the CARS signal in the transients recorded for the parallel and perpendicular polarization geometries in Fig. 10a and b shows a fast modulation with a period of 433 and 439 fs, respectively. The Fourier transformation of these transients in Fig. 11a and b show that this period corresponds to an energy spacing of approximately $77\,\mathrm{cm}^{-1}$. This is in agreement with the energy spacing between the vibrational eigenstates of gaseous iodine in the excited B state accessed by the time-variable laser pulse with $\lambda_{pu_\tau} = 560\,\mathrm{nm}$ and, as discussed in Sect. 3.1, this fast modulation of the CARS signal can be attributed to the vibrational dynamics in the excited B state of iodine.

Furthermore, a slow modulation in the intensity of the CARS signal can also be observed in the transients in Fig. 11a and b for a parallel and perpendicular polarization geometry, respectively. The slow modulation is most evident for delay times Δt between 0 and -5 ps and corresponds to the low-frequency component between 2 and $12\,\mathrm{cm}^{-1}$ in the respective Fourier transformation of both the transients. The contribution of the slow modulation to the overall CARS signal can be emphasized with the help of the corresponding Fourier transformation. By eliminating all the high-frequency components in the Fourier transformation and solely transforming the frequency components between 2 and $12\,\mathrm{cm}^{-1}$

Fig. 11a–c. An FFT of the respective femtosecond CARS transients in Fig. 10 recorded under a **a** parallel, **b** perpendicular, and **c** magic-angle polarization geometry

back into the time domain, a curve is obtained that is superimposed as a solid line on the respective CARS transients in Fig. 10a and b (compare Figs. 5–8).

This slow modulation in both transients (Fig. 10a and b) can be attributed to the coherent rotational dynamics of iodine in the excited B state. The modulation of the CARS signal due to the rotational dynamics of the iodine ensemble is caused by the dependence of the probability P of excitation into an excited state on the orientation of the electrical field vector $\boldsymbol{E}$ of the inducing laser to the transition dipole moment $\boldsymbol{\mu}$ of the molecular system [83].

Due to this orientational dependence, the time-variable laser pulse pu_τ, which interacts with the system first, prepares an ensemble of iodine molecules which all have an orientation in space determined by the orientation of the electrical field vector of the inducing laser field. This selected ensemble is then probed after the delay time Δt with the simultaneous laser pulses pu and S having equal polarization. The resulting CARS signal is now modulated with the continuous change of the dipole moment orientation of the rotating iodine molecules to the electrical field of the simultaneous laser pulses pu and S.

In the transient recorded with a parallel polarization geometry, at time zero the orientation of the ensemble of iodine molecules which is initially prepared by the time-variable pump pulse pu_τ is probed with parallel polarization of the laser pulses pu and S. Therefore, the signal shows a maximum at time zero ($\Delta t = 0$) and decreases in intensity in the first few picoseconds. The latter is caused by the rotation of the iodine molecules out of the initially selected orientation. In the case of the perpendicular polarization geometry, the starting conditions are the same, but the probing is done with vertical laser polarizations relative to the dipole moment orientation at time zero. This results in a minimum signal for $\Delta t = 0$ followed by an increasing intensity. This rise of the signal is the result of the ensemble rotating towards the orientation of the polarization of the probing laser pulses. In both the parallel and the perpendicular polarization geometry, the initial modulation of the CARS signal due to the rotational dynamics levels out to a nearly constant intensity in the delay time Δt between -3 and -20 ps. This is due to the distribution of the iodine molecules over a large spectrum of rotational eigenstates in the initially selected ensemble. Because of this, the molecules in the ensemble rotate with a different angular velocity causing the original, nearly consistent orientation of the ensemble to spread to a homogeneous distribution over all orientations in space. The rotational revivals which are observed due to the fact that all the energies of rotational eigenstates possess the rotational constant B as a common multiple are not seen in these measurements since they occur at delay times not accessed here [67].

With the help of the well-known magic-angle polarization geometry [41, 72, 73, 83, 84], it is possible to eliminate this slow modulation resulting from the rotational dynamics and allow the observation of the vibrational dynamics unperturbed by rotational effects. The magic angle of $54.7°$ between pu_τ and the simultaneous pu and S laser pulses results in a weighted superposition of contributions probed under parallel and perpendicular polarization conditions such that $2I_\perp = I_\parallel$. Since the two equally weighted parts are opposite in their phase, this superposition leads to a destructive

interference and subsequently an elimination of the rotational effects from the transient CARS signal.

The transient recorded under these conditions is shown in Fig. 10c. The Fourier transformation of this transient in Fig. 11c confirms the elimination of the rotational modulation out of the signal with the absence of a frequency component between 2 and 12 cm^{-1}. The straight solid line superimposed on to the measurement emphasizes that the fast modulation of the CARS signal does not have the slow modulation superimposed resulting from rotational dynamics. The transient under magic-angle conditions allows for the characterization of a damping in the amplitude of the vibrational oscillations due to anharmonicity as well as rotational–vibrational interaction leading to a loss of vibrational coherence [48].

The magic-angle geometry also suppresses the contribution of rotational dynamics to ground-state FWM transients. This is discussed in detail in [55].

3.3 The laser wavelengths

Similar to the FWM spectroscopies in the frequency domain, in the time domain the laser wavelengths also determine the nonlinear process. In principle one has to consider two main points: (i) the wavelengths of the lasers generating the non-linear response of the system by a certain FWM method (e.g. CARS) can be resonant or nonresonant with transitions between electronic and/or ro-vibrational states of the molecules, (ii) by changing the wavelength ratio of the three lasers involved, different FWM processes take place. Here, we consider CARS, DFWM, and CSRS (see Fig. 1).

3.3.1 Molecular resonances. In Sect. 3.1–Sect. 3.2, we have already discussed that the wavelengths of the lasers determine at which energy position and on which PES wave packets are prepared. Basically, two types of resonances can be distinguished. First, 'electronic resonances' where laser pulses are in resonance with a transition between different electronic states of the molecules (in our case, in the visible to UV spectral range). These resonances are responsible for the excited-state wave packets. If the lasers are nonresonant with electronic transitions, no excited-state dynamics contribute to the transient signal. Second, 'Raman resonances', which are two-photon (pump–dump) resonances with ro-vibrational levels in the electronic ground state of the molecules and which determine where a coherent ground-state excitation takes place.

Each of these resonances results in an enhancement of the FWM signal. But these resonances are not mandatory for the nonlinear process to take place. As the femtosecond laser pulses are spectrally broad, in practically all cases Raman resonances have to be considered. However, electronic resonances may not contribute due to the high absorption energies of many molecules, where excitation wavelengths in the UV are required to meet an absorption transition. Examples for such nonresonant femtosecond FWM spectroscopy are given in Sect. 3.5.1.

As an example of the influence of the laser wavelength on the molecular dynamics in the electronic excited state, CARS transients are shown in Fig. 12 which were taken with different pump-laser wavelengths; an example for changed Raman resonances is given in Fig. 9. The wavelength is varied within the bound portion of the B state of iodine (620 to 536 nm).
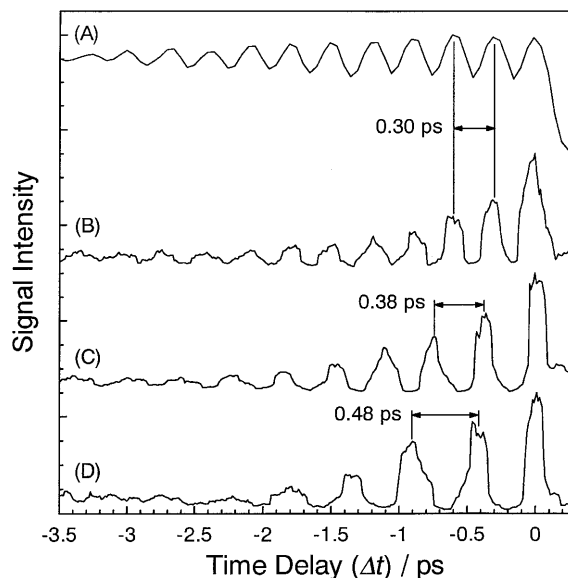
Fig. 12. Femtosecond pump–probe (A) and CARS transients for different pump-laser wavelengths (B–D). (A) pump–probe ($\lambda_{pu} = 620$ nm, $\lambda_{pr} = 310$ nm) with detection of laser-induced fluorescence (LIF) ($\lambda_{LIF} = 340$ nm). CARS transients for (B) $\lambda_{pu} = \lambda_{pu_\tau} = 620$ nm, $\lambda_S = 645$ nm, $\lambda_{aS} = 596$ nm; (C) $\lambda_{pu} = \lambda_{pu_\tau} = 559$ nm, $\lambda_S = 579$ nm, $\lambda_{aS} = 539$ nm; (D) $\lambda_{pu} = \lambda_{pu_\tau} = 536$ nm, $\lambda_S = 554$ nm, $\lambda_{aS} = 518$ nm

Through this, the wave packets are prepared at different mean vibrational quantum numbers [85]. We observe different periods in the coherent evolution of wave packets in the B state. Curve A of Fig. 12 shows the femtosecond pump–probe signal ($\lambda_{pu} = 620$ nm, $\lambda_{pr} = 310$ nm) where laser-induced fluorescence (LIF) at $\lambda_{LIF} = 340$ nm was detected (compare e.g. to results obtained in [85]). With curves B to D in Fig. 12, we show a selection of the CARS transients for three different wavelength combinations: B ($\lambda_{pu} = \lambda_{pu_\tau} = 620$ nm, $\lambda_S = 645$ nm, $\lambda_{aS} = 596$ nm), C ($\lambda_{pu} = \lambda_{pu_\tau} = 559$ nm, $\lambda_S = 579$ nm, $\lambda_{aS} = 539$ nm), and D ($\lambda_{pu} = \lambda_{pu_\tau} = 536$ nm, $\lambda_S = 554$ nm, $\lambda_{aS} = 518$ nm). We found that the period of the oscillation increases as the pump energy is increased. The CARS transients show oscillations with an average period of 300, 380, and 480 fs for the B, C, and D transients, respectively. Calculations of these oscillation periods have also been made using the available spectroscopic data of the B state, and good agreement was found between the calculated and observed periods [86]. In Fig. 12, curves A and B, we compare the result of the nonlinear femtosecond CARS gas-phase technique (curve B) with that obtained by the conventional pump–probe technique using LIF detection (curve A) [85, 87]. Excellent agreement is found for the period of the oscillations as well as for the decay of the amplitudes between the two transients, the latter being taken with the same pump wavelength ($\lambda_{pu} = \lambda_{pu_\tau} = 620$ nm). This observation points to the same decay mechanism (vibrational dephasing, rotational relaxation) for the CARS process compared to the pump–probe experiment if $\Delta t < 0$ [73]. In contrast to the pump–probe experiments, in the CARS experiment no contributions from other electronically excited states [85] could be detected. This is due to the high selectivity of the FWM process.

3.3.2 Four-wave-mixing processes. In the frequency domain, FWM spectroscopy is a well-established technique, which

was first demonstrated by Terhune and Maker [88, 89]. CARS and DFWM are the most important FWM processes and are described in detail in several books [90–92]. The introduction of time resolution into the FWM process gives these techniques a new meaning and again CARS and DFWM play a dominant role [5, 6, 26–28, 31–33, 93]. There are relatively few applications of time-resolved CSRS [29]. The different FWM techniques are determined by the wavelength ratio of the three lasers interacting with the molecular system (see Fig. 1).

In Fig. 13, we compare the results from femtosecond time-resolved CARS, DFWM, and CSRS spectroscopy on iodine. It is obvious that drastic changes in the transient shape occur, pointing to the fact that the different FWM techniques excite and record different molecular dynamics.

The femtosecond CARS experiment was already discussed in detail in Sect. 1–3.2. Here, two laser pulses (pu and pu_τ) have the same wavelength, $\lambda_{pu} = \lambda_{pu_\tau} = 620$ nm. The third laser pulse (S) is tuned to $\lambda_S = 645$ nm. The laser pulses pu and S are coincident in time. The transient in Fig. 13a is the CARS signal as a function of delay time between the pulse pair (pu, S) and the second pump laser pu_τ. For negative delay times ($\Delta t < 0$), the transient signal oscillates with a period of about 300 fs, which corresponds to a wavenumber difference of approximately 111 cm^{-1}. This is exactly the energy spacing of the vibrational states which are coherently excited by a 620 nm transition B←X in iodine. As the

energy difference between pu and S results in a Raman resonance with the vibrational eigenstate around $v'' = 3$ in the ground X state, wavenumber spacings of about 210 cm^{-1} can be expected [64]. In effect, the oscillations found for positive delay times ($\Delta t > 0$) have a period of 160 fs, corresponding to 208 cm^{-1}.

The DFWM transient discussed in the following was recorded using three laser fields having the same central wavelength λ_0, which is resonant with ro-vibrational eigenstates in the excited B state of iodine. While two laser pulses (pu_1 and pu_2) are coincident in time the third pulse (pu_τ) arrives with a variable time delay. Figure 13b shows a typical DFWM transient of iodine as a function of the delay time Δt between the variable laser pulse, pu_τ, and the fixed pulse pair (pu_1, pu_2). The transient exhibits well-defined 300 fs beats, corresponding to a vibrational energy spacing of about 111 cm^{-1}. This agrees well with the experimental vibrational energy spacings in the excited B state of gaseous iodine accessed by the 620 nm lasers. For positive delay times ($\Delta t > 0$) additional beats having about twice this wavenumber appear. These oscillations show a period of 155 fs, which corresponds to an energy spacing of 215 cm^{-1} and reflects the dynamics of a wave packet within the electronic ground state of iodine.

The femtosecond CSRS transient displayed in Fig. 13c shows a completely different time behaviour than the CARS (see Fig. 13a) or the DFWM transient (see Fig. 13b). In the femtosecond CSRS experiment three laser fields also interact with the ensemble of iodine molecules. Two laser pulses have the same wavelength, $\lambda_{pu} = \lambda_{pu_\tau}$, and further on will be referred to, in consistency with the CARS experiment, as pump lasers. The third laser (anti-Stokes) is tuned, in contrast to the CARS experiment, to a shorter wavelength, λ_{aS}, such that the difference between pump- and anti-Stokes-laser wavelengths is resonant with a vibrational transition in the ground state. Figure 13c shows the fs CSRS transient as a function of the delay time Δt between the pulse pu_τ and the two time-coincident pulses pu and aS. For a pump wavelength $\lambda_{pu} = \lambda_{pu_\tau} = 615$ nm and an anti-Stokes wavelength $\lambda_{aS} = 591$ nm the coherent Stokes signal is detected at $\lambda_S = 641$ nm. As is the case for the CARS transient, here also the wavelengths of the pump lasers pu and pu_τ determine where the interaction with the excited-state potential takes place. The difference between the wavelengths of pump (pu) and anti-Stokes (aS) lasers ($\lambda_{aS} - \lambda_{pu}$), which was chosen to be resonant with the second overtone $\Delta v'' = 3$ within the ground state of the iodine molecules, gives the position accessed in the ground-state potential. The transient shows neither a signal nor a beating structure for negative delay times ($\Delta t < 0$). For positive delay times ($\Delta t > 0$) the transient exhibits well-defined 320 fs beats, corresponding to a vibrational energy spacing of about 104 cm^{-1}. This agrees well with the vibrational energy spacings in the excited B state of gaseous iodine accessed by the 615 nm pump laser. Also, beats having about twice this wavenumber appear. These can be assigned to the electronic ground state. The FFT spectrum of the CSRS transient (not shown in this paper) also exhibits two distinct components at 111 and 208 cm^{-1}. The peak at 111 cm^{-1} can be assigned to the vibrational coherences in the B state of iodine, while the peak at 208 cm^{-1} corresponds to the second overtone ($\Delta v'' = 3$) of iodine in the electronic ground state. That is exactly what could be expected from the experimental conditions as mentioned above.
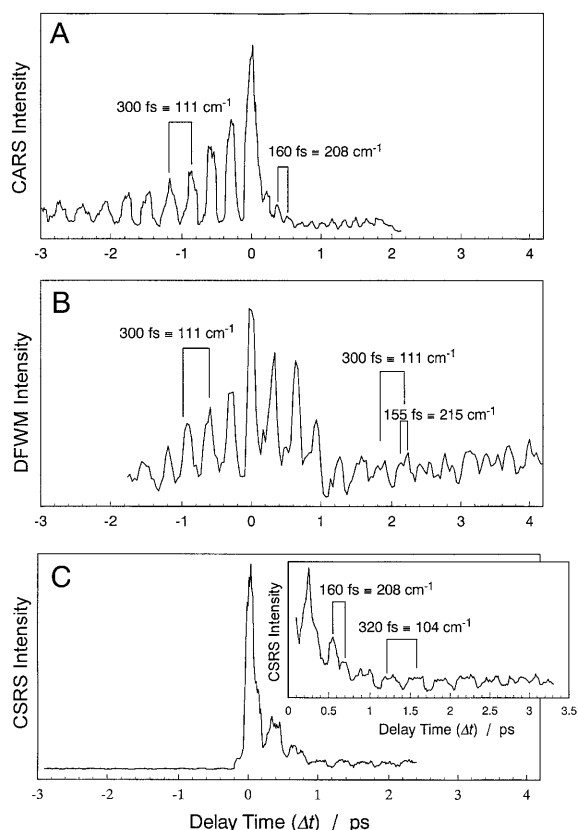
**Fig. 13a–c.** Femtosecond FWM transients of gaseous iodine: **a** femtosecond CARS transient ($\lambda_{pu} = \lambda_{pu_\tau} = 620$ nm, $\lambda_S = 645$ nm, $\lambda_{aS} = 596$ nm); **b** femtosecond DFWM transient ($\lambda_{pu_1} = \lambda_{pu_2} = \lambda_{pu_\tau} = \lambda_{DFWM} = 620$ nm); **c** femtosecond CSRS transient ($\lambda_{pu} = \lambda_{pu_\tau} = 615$ nm, $\lambda_{aS} = 591$ nm, $\lambda_S = 641$ nm)

Theory helps us to understand the dependence of the observed dynamics on the timing of the laser pulses as well as the variation of the laser wavelengths resulting in the different FWM techniques. The nonlinear polarization responsible for the FWM signal can be theoretically described using the density-matrix formalism. An elegant method for calculating the elements of the involved density matrix is using time-evolution energy ladder diagrams according to Lee and Albrecht [94, 95]. These diagrams include a time ordering of the possible interactions as well as information about the interactions themselves. The nonlinear susceptibility or polarization is derived by summing all possible diagrams. If spectroscopic results in the frequency domain are described by this technique, a selection of important diagrams can be performed on the basis of resonance conditions. This means that the choice of laser frequencies (different FWM techniques) together with the molecular transition determine which diagrams are of importance and which are not. For the femtosecond time-resolved experiments on systems which show coherences much longer than the pulse durations (as is the case for iodine vapour used in the above-described experiments), the timing of the laser pulses additionally selects diagrams which have the right time ordering.

Figure 14 shows the time-evolution diagrams that illustrate the contributions for the three FWM processes (CARS, DFWM, CSRS) for negative [diagrams (A) and (B)] and positive [diagrams (C)–(E)] delay times. For simplicity, we neglect in our discussion diagrams starting with transitions

from thermally occupied higher vibrational ground-state levels. With the help of these diagrams, one can determine in which electronic state (ground X state or excited B state) the wave packet is generated by the laser pulse(s) that interact(s) with the system first. From this, one can conclude whether the dynamics of the electronic ground X or the excited B state are monitored by the time-dependent FWM signal.

In the case of the femtosecond time-resolved DFWM process pu_τ prepares a wave packet in the B state for negative delay times ($\Delta t < 0$). Therefore, the time-dependent DFWM signal reflects the dynamics of the excited B state. This is characterized by diagrams (A) and (B). For positive delay times ($\Delta t > 0$) a superposition of the ground- and B-state dynamics can be observed in the resulting DFWM transient signal. This corresponds to diagrams (C)–(E), which demonstrate the preparation and subsequent DFWM signal of vibrational coherences in the ground state as well as the excited B state. Diagrams (C) and (E) illustrate the motion of a wave packet in the electronic ground state. This wave packet is prepared by the laser pulses pu_1 and pu_2, which interact simultaneously with the iodine molecules. On the other hand, diagram (D) illustrates the dynamics of a wave packet in the excited B state, which is prepared by an excitation similar to a 'two-photon' absorption by pu_1 and pu_2. The quantitative contribution of each diagram to the total DFWM signal can only be determined by means of quantum-mechanical calculations. Such calculations were performed by Meyer et al. [46, 47, 53, 96] and show excel-
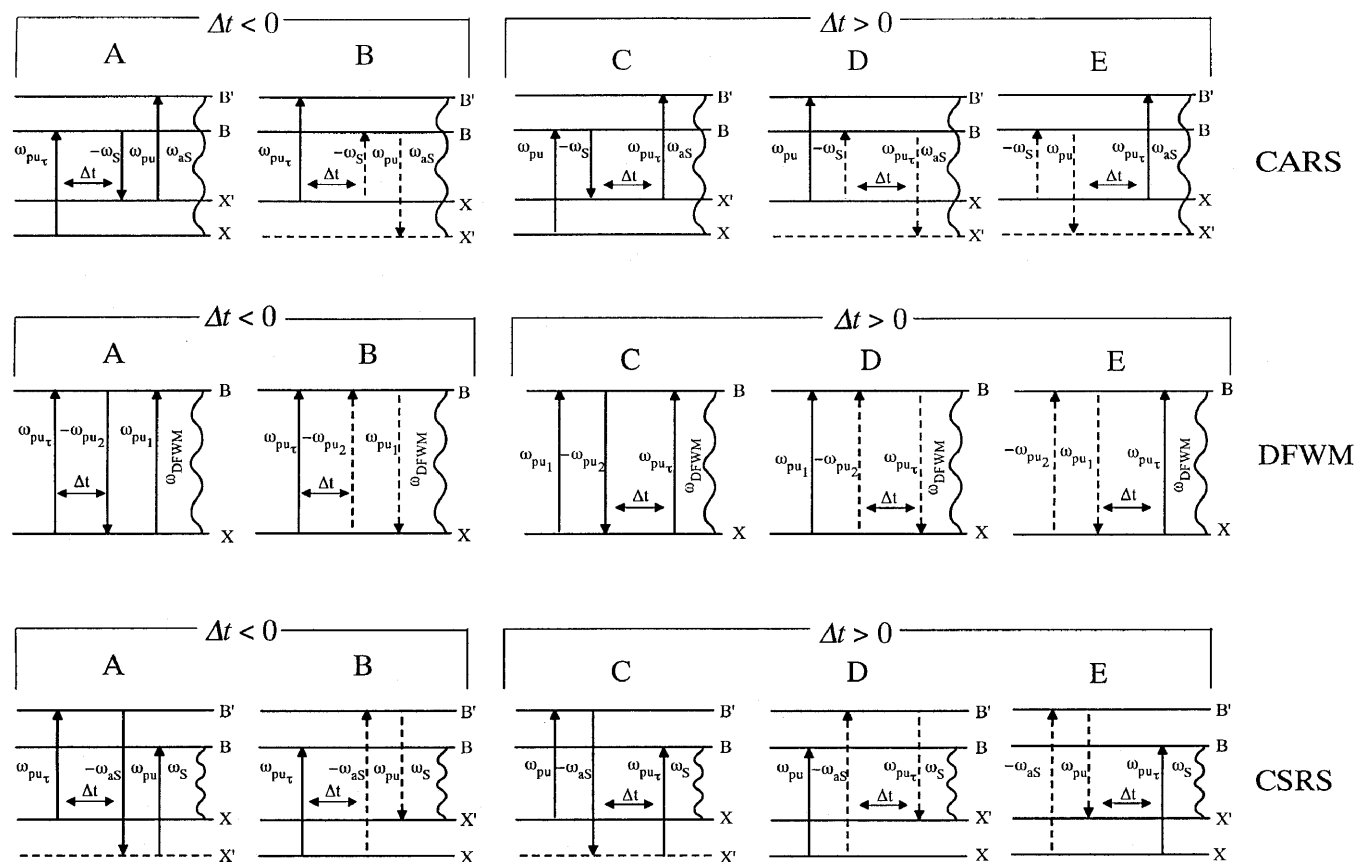
Fig. 14. Time-evolution diagrams describing the femtosecond time-resolved FWM processes CARS, DFWM, and CSRS for $\Delta t < 0$ [(A) and (B)] and $\Delta t > 0$ [(C)–(E)]. The *solid* and *dashed arrows* represent a ket and a bra side transition, respectively. See [94, 95] for details

lent agreement between the experimental and the calculated transients.

The situation is more complicated for the coherent Raman techniques CARS and CSRS due to the nondegeneracy of the laser and signal wavelengths. The diagrams (A) and (B) corresponding to the CARS process for negative delay times ($\Delta t < 0$) reflect the dynamics of a wave packet prepared by pu_τ in the B state of iodine. The main contribution to the transient CARS signal for $\Delta t < 0$ is given by diagram (A) because diagram (B) shows in contrast to diagram (A) no Raman resonance. If positive delay times ($\Delta t > 0$) are chosen both pu and S excite the molecules, which afterwards are probed by pu_τ.

Diagrams (C) and (E) reflect the ground-state dynamics in the CARS signal, while diagram (D) shows that B-state dynamics contributes to the nonlinear signal. However, diagram (C) will dominate the CARS signal for positive delay times due to the missing Raman resonance in the diagrams (D) and (E).

Therefore, the femtosecond CARS signal for $\Delta t < 0$ is mainly determined by diagram (A) and for $\Delta t > 0$ diagram (c) plays the main role. This is in excellent agreement with the experimental CARS transient (Fig. 13a) where for negative delay times ($\Delta t < 0$) the wave packet dynamics in the B state [diagram (A)] and for positive delay times the ground-state dynamics [diagram (C)] of iodine can be resolved. Quantum-mechanical calculations by Meyer et al. [46, 47, 53, 96] confirmed that for negative delay times mainly diagram (a) and for positive delay times mainly diagram (C) contribute to the transient CARS signal.

The time-dependent CSRS signal for negative delay times ($\Delta t < 0$) should reflect the dynamics of the excited B state. This is characterized by diagrams (A) and (B), where diagram (B) plays the main role because of the missing Raman resonance in diagram (A).

For positive delay times the diagrams (C) and (E) show that wave packet dynamics in the electronic ground state should contribute to the transient signal, which was initiated by the simultaneous interaction with pu and aS. Again, diagram (C) will play a minor role, due to the fact that it shows no Raman resonance. On the other hand diagram (D) illustrates the dynamics of a wave packet in the excited B state, which is prepared by an excitation similar to a two-photon absorption by pu and aS. From this the femtosecond CSRS transient should reflect the dynamics of the B state for $\Delta t < 0$ [diagram (B)] and for $\Delta t > 0$ a superposition of the ground- [diagram (E)] and B-state [diagram (D)] dynamics should be observed in the resulting CSRS transient signal. The assumption for positive delay times ($\Delta t > 0$) is consistent with the experimental results (see Fig. 13c). However for negative delay times ($\Delta t < 0$) no signal at all could be observed in the experimental transient. So the influence of diagram (B) in comparison to the diagrams (D) and (E) seems to be negligible. Only precise quantum-mechanical calculations can determine the quantitative contributions of each diagram. Such calculations are under way and will be published in due course.

3.4 The detection wavelength

In the experiments described before, the detection wavelength was chosen according to the frequency-domain measurements. This means that a narrow spectral window was opened

by the monochromator which was centred at a position which can be calculated from the energy-conservation conditions of the respective FWM processes. For example the CARS detection wavenumber would be $\tilde{v}_{aS} = \tilde{v}_{pu_\tau} + (\tilde{v}_{pu} - \tilde{v}_S)$, where $\tilde{v}_{pu_\tau}$, $\tilde{v}_{pu}$, and $\tilde{v}_S$ are the *central wavenumbers* of the according laser pulses. However, the fs pulses are spectrally broad. Therefore, the resulting FWM signal is not a spectrally narrow line but rather a broad band. Each spectral component of this signal light field is generated by different laser-pulse contributions where energy conservation has always to be obeyed. Thus, by varying the detection window one would expect to see different dynamical information from the molecular system in nonlinear response to the FWM process.

In the following, we demonstrate for the femtosecond DFWM process on iodine molecules that changing the spectral detection window results in completely different transient behaviour. An example of the interesting information which can be extracted from the signal band in the case of femtosecond CARS spectroscopy will be given in Sect. 3.5.

The three laser fields interacting with the ensemble of iodine molecules all have the same wavelength $\lambda_0 = 573$ nm ($\tilde{v}_0 = 17\,452$ cm^{-1}). Two pulses (pu_1, pu_2) are coincident in time ($t = 0$) and the third pulse (pu_τ) arrives with a variable delay time Δt. Depending on the relative timing of the three pulses as well as the detection wavelength, different dynamics in the molecules are probed by one- or two-photon interaction resulting in the coherent FWM signal. This is shown in panels A of Figs. 15–17 for different detection wavelengths as indicated in the respective panels D (the spectral widths of the pulses employed in our experiments were about 250–300 cm^{-1}).

If the detection wavelength equals the centre wavelength of the laser pulses, the time behaviour which results from a DFWM process can be observed (compare Sect. 3.3). The transient (Fig. 15a: $\lambda_{det} \approx \lambda_0$) exhibits well-defined beats with a separation of about 350 fs, corresponding to a vibrational energy spacing of about 94 cm^{-1}. This agrees well with the vapour-phase vibrational energy spacings in the excited B state accessed by the 573 nm lasers from the electronic and vibrational ground state.

Recently Yang et al. [32] reported results on time-resolved DFWM experiments on iodine vapour using nanosecond laser
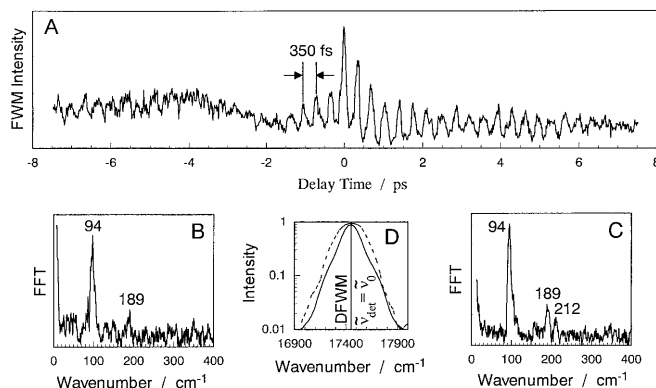

Fig. 15. a Femtosecond FWM transient for DFWM conditions: detection at the central wavenumber position of the laser pulses ($\tilde{v}_{det} = \tilde{v}_0$). **b** and **c** are the FFT spectra obtained for negative and positive delay times, respectively. **d** FWM signal for $\Delta t = 0$ (*full line*) and laser pulse shape (*dashed line*) with detection wavenumber position marked

pulses. In contrast to our experiments they varied the time between two excitation pulses on a femtosecond time scale while for the probe pulse a constant delay time of more than 10 ns was chosen. They observed a transient signal with beats having a frequency characteristic for the spacing between vibrational levels of the B state near the centre laser frequency. The rate of decay of the beats and the symmetry of the signal with respect to $\Delta t = 0$ were consistent with the assumption that rotational energy randomization had taken place during the 10–20 ns waiting time between excitation and probe pulses. These authors also gave a theoretical expression describing the transient which results if neither the vibrational nor the rotational coherences are lost during the waiting time for the third pulse (which is the case in a corresponding experiment using femtosecond laser pulses). The calculated DFWM transient clearly shows beats at the excited-state vibrational frequency, as well as weak features at about twice this frequency, which can be assigned to ground-state vibrational beats. Furthermore, the calculated signal is significantly asymmetric with respect to $\Delta t = 0$.

The theoretical transient including the rotational and vibrational coherences (see Fig. 5 of [32]) has an appearance quite similar to our experimental DFWM result shown in Fig. 15a. In our experiment we used two pulses, which are coincident in time ($pu_1(\tilde{\nu}_0)$ and $pu_2(\tilde{\nu}_0)$) and a third pulse ($pu_\tau(\tilde{\nu}_0)$) which is variable in time. The delay times in our experiments range from −8 to 8 ps. For negative delay times $\Delta t < 0$ the laser pulse pu_τ excites the molecular system and the pulses pu_1 and pu_2 act as probe. If positive delay times are chosen both pu_1 and pu_2 excite the molecules, which afterwards is probed by pu_τ. During the short delay times applied in our experiments, a vibrational or rotational energy randomization has not taken place which makes the similarity between the calculations by Yang et al. [32] and our experiments appear reasonable. In order to analyse our experimental data more closely, we show the results of an FFT of the transient given in Fig. 15a, in Fig. 15b and c for negative ($\Delta t < 0$) and positive delay times ($\Delta t > 0$), respectively. For negative delay times the FFT spectrum (Fig. 15b) of the DFWM transient (Fig. 15a) exhibits a vibrational peak at about $94\,\mathrm{cm}^{-1}$. As mentioned above, this value agrees with the energy spacings of the vibrational levels accessed in the B state of iodine. One also finds a weak feature at about $189\,\mathrm{cm}^{-1}$ which is the second harmonic belonging to the $94\,\mathrm{cm}^{-1}$ band. For positive delay times (Fig. 15c) an additional vibrational peak at about $212\,\mathrm{cm}^{-1}$ occurs in the FFT spectrum. This wavenumber position agrees with the fundamental vibrational transition ($\Delta v'' = 1$) of iodine in the ground state.

If we now choose a wavelength of $\lambda_\mathrm{det} = 565\,\mathrm{nm}$ ($\tilde{\nu}_\mathrm{det} = 17\,699\,\mathrm{cm}^{-1}$) for detection, the shape of the resulting transient changes considerably (Fig. 16a). For negative delay times $\Delta t < 0$ the beat patterns have the frequency of the wave packet in the excited B state of iodine. For positive delay times ($\Delta t > 0$) the beats have about twice this frequency and can be assigned to the electronic ground state. This also becomes evident from the FFT performed on the transient shown in Fig. 16a. Figure 16b and c of this figure show the FFT spectra for negative and positive delay times, respectively. The FFT spectrum for $\Delta t < 0$ (Fig. 16b) exhibits a line at about $94\,\mathrm{cm}^{-1}$, which is the vibrational energy spacing in the excited B state. Additionally, the second harmonic of this wavenumber can be seen at about $189\,\mathrm{cm}^{-1}$. For $\Delta t > 0$
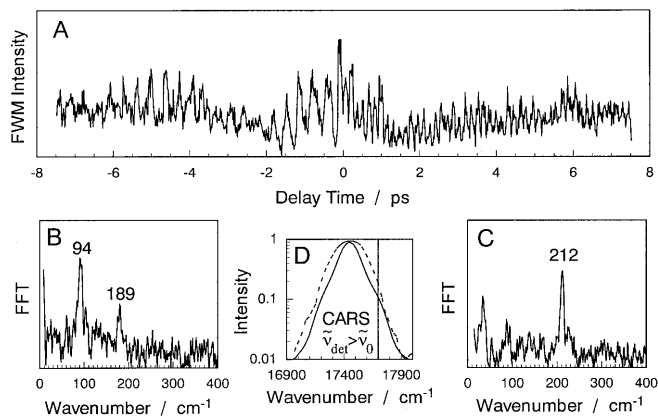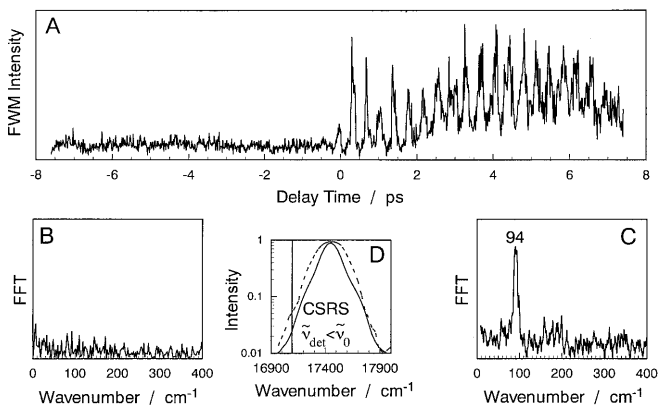

Fig. 16. Same as Fig. 15 except for having CARS conditions: detection at a wavenumber position anti-Stokes-shifted relatively to the centre of the pulse shapes ($\tilde{\nu}_\mathrm{det} > \tilde{\nu}_0$)

the FFT spectrum (Fig. 16c) shows only one peak at about $212\,\mathrm{cm}^{-1}$ which again can be assigned to the fundamental vibrational transition $\Delta v'' = 1$ of iodine in the ground state.

This behaviour can be easily explained by assuming a FWM process which is favoured by the choice of an anti-Stokes detection wavenumber $\tilde{\nu}_\mathrm{det} > \tilde{\nu}_0$ (compare Fig. 16d). The corresponding FWM process is CARS. Here, we have $pu_\tau(\tilde{\nu}_\mathrm{det} - \Delta\tilde{\nu})$ as time-variable pump pulse. The pulses $pu_1(\tilde{\nu}_\mathrm{det} - \Delta\tilde{\nu})$ and $pu_2(\tilde{\nu}_\mathrm{det} - 2\Delta\tilde{\nu})$ act as second pump and Stokes lasers, respectively. $\Delta\tilde{\nu}$ actually can assume any value within the spectral range of the involved laser pulses (starting from $\tilde{\nu}_\mathrm{det}$). However, the process will be dominated by contributions where the laser intensities at ($\tilde{\nu}_\mathrm{det} - \Delta\tilde{\nu}$) and ($\tilde{\nu}_\mathrm{det} - 2\Delta\tilde{\nu}$) as well as the transition probabilities between the states involved are high.

Instead of choosing a detection wavelength on the anti-Stokes side of the central laser wavelength $\lambda_0 = 573\,\mathrm{nm}$ ($\tilde{\nu}_0 = 17\,452\,\mathrm{cm}^{-1}$) it is of course also possible to set the monochromator to a position on the Stokes side. In the following we show results obtained for a detection wavelength $\lambda_\mathrm{det} = 585\,\mathrm{nm}$ $\tilde{\nu}_0 = 17\,094\,\mathrm{cm}^{-1}$) which lies in the edge of the spectral range of the laser pulses (compare Fig. 17d). The FWM process which is favoured by the Stokes detection is the CSRS. Here, we have $pu_\tau(\tilde{\nu}_\mathrm{det} + \Delta\tilde{\nu})$ as time-variable pump

Fig. 17. Same as Fig. 15 except for having CSRS conditions: detection at a wavenumber position Stokes-shifted relatively to the centre of the pulse shapes ($\tilde{\nu}_\mathrm{det} < \tilde{\nu}_0$)

pulse. The pulses $pu_1(\tilde{\nu}_{det} + \Delta\tilde{\nu})$ and $pu_2(\tilde{\nu}_{det} + 2\Delta\tilde{\nu})$ act as second pump and anti-Stokes lasers, respectively. As for the CARS process described above, $\Delta\tilde{\nu}$ can take any value within the spectral range of the involved laser pulses (starting from $\tilde{\nu}_{det}$). The main contributions will now be determined by maximum laser intensities at $(\tilde{\nu}_{det} + \Delta\tilde{\nu})$ and $(\tilde{\nu}_{det} + 2\Delta\tilde{\nu})$ as well as the transition probabilities between the states involved in the CSRS process.

The transient obtained under such conditions is shown in Fig. 17a. Now, the transient shows neither signal nor beating structures for negative delay times $\Delta t < 0$. However, for $\Delta t > 0$ intense beat patterns can be found at the excited B-state vibrational frequency. This is also demonstrated by the FFT spectra shown in Fig. 17b and c, which were obtained from the transient for negative and positive delay times, respectively. While for $\Delta t < 0$ the FFT does not exhibit any dominating frequency contribution, the frequency spectrum describing the coherence probed for $\Delta t > 0$ has an intense band at about $94\,cm^{-1}$ and possibly a very small contribution at the second-harmonic position ($\approx 189\,cm^{-1}$) as well as at the ground-state wavenumber ($\approx 212\,cm^{-1}$).

3.5 Application: ground-state dynamics in larger systems

Especially for more-complex molecular systems it is interesting to gain information about the ground-state dynamics. Several time-resolved techniques can be used for this purpose, like transient absorption bleaching or anti-Stokes Raman spectroscopy. The nonlinear FWM spectroscopy seems to be the obvious method for gaining ground-state information: (i) no knowledge about electronic excited states is necessary, as no electronic resonance is required for the FWM process, (ii) due to the phase-matching condition which is inherent to this technique, a laser-like signal of considerably high intensity arises, which is in principle free of background, (iii) the many degrees of freedom can be used to gain additional information compared to other methods (e.g. isotropic *vs.* anisotropic contributions, etc.). The main disadvantage might be the relatively complicated experimental set-up which is required for any FWM experiment. In the following, we present two examples where femtosecond time-resolved FWM was applied to gain information about rovibrational dynamics in the electronic ground state of larger molecules.

3.5.1 Binary gas-phase mixtures. First, we would like to discuss femtosecond CARS experiments performed on benzene, toluene, and their binary mixtures in the gas phase. In each case a sample cell containing the liquids (for the binary system a 1:1 mixture of benzene and toluene) was slightly heated to $\approx 80\,^\circ C$. Under these conditions, the gaseous mixture of benzene and toluene was about 2:1 (see above). For the Raman excitation, a wavenumber difference of $\tilde{\nu}_{pu} - \tilde{\nu}_S = 1000\,cm^{-1}$ between pump and Stokes lasers was chosen. Due to the spectral width of the femtosecond exciting lasers of more than $200\,cm^{-1}$, several modes were coherently excited in the molecules. The main vibrational modes in benzene are the ring-breathing mode of benzene [97] ($^{12}C_6H_6$) and of benzene with one carbon-13 ($^{13}C^{12}C_5H_6$) present at natural abundance [6] at 992 and $984\,cm^{-1}$, respectively. The wavenumbers of the excited Raman transitions in toluene are

788, 1001, and $1028\,cm^{-1}$. These can be assigned to the ring-breathing mode and ring-deformation modes of toluene, respectively (see [97] and references cited therein). A spontaneous Raman spectrum of the binary mixture in Fig. 18 shows these vibrational modes. We would like to emphasize that no electronic resonance was involved in this FWM process as electronic transitions are in the UV spectral region for benzene as well as toluene.

Figure 19 shows the results of the femtosecond CARS experiments. Together with the experimental transients, results of quantum calculations are displayed in this figure which reproduce the general features of the measured data. For a detailed description of the theoretical simulations we refer to [49]. For the transients taken from toluene and the binary
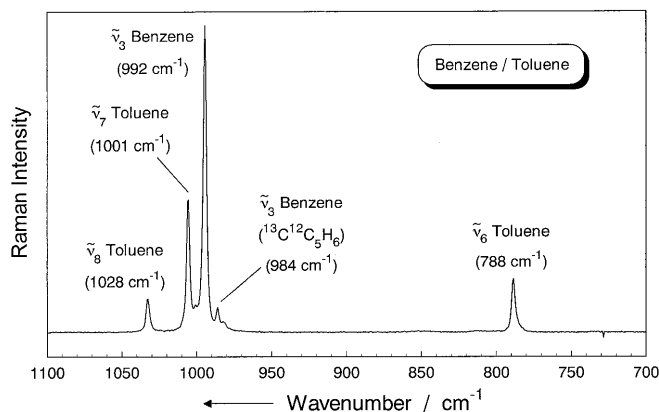
Fig. 18. Raman spectrum of a binary 1:1 mixture of benzene and toluene. The different modes are labelled
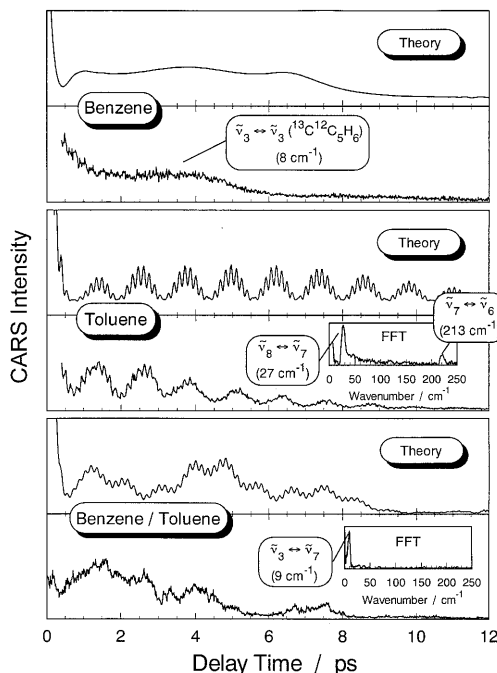
Fig. 19. Femtosecond CARS transients taken of benzene, toluene, and a mixture of benzene and toluene in the gas phase. The experimental data are shown together with results of quantum calculations [49]. For toluene and benzene/toluene FFTs of the experimental transients are shown as *inserts*

mixture of benzene and toluene results from FFT calculations are shown in inserts.

For benzene, the CARS process excites a single vibrational level. This is due to the laser pulses that have a temporal width (full width at half maximum, FWHM) of 80 fs. Therefore, *pu* and *S* only can access the ring-breathing mode which lies at 992 cm^{-1} in benzene and at 984 cm^{-1} in $^{13}C^{12}C_5H_6$. Again, the signal is obtained from a mixture of 94% $^{12}C_6H_6$ and 6% $^{13}C^{12}C_5H_6$ according to the natural abundance of ^{13}C. The time difference between the two minima seen in the modulation of the transient CARS signal corresponds to a beat frequency between the two isotopes.

A different situation as for benzene is encountered in the toluene system, as can be seen in Fig. 19. The same experimental conditions were used as for the benzene CARS experiment. However, in this case several vibrational levels can be excited coherently through the interaction with the first two laser pulses *pu* and *S*. The preparation of a vibrational wave packet composed of several eigenstates for the vibrational degrees of freedom results in quantum beats in the CARS signal, as can be seen in the figure which shows the experimentally obtained femtosecond CARS transient together with a FFT. Several oscillations appear which clearly belong to the vibrational energy differences in the toluene molecule. The signal would not exhibit any decay and oscillate with the same amplitudes for infinite times if the rotational dynamics did not contribute to the nonlinear FWM response.

It is interesting to discuss the CARS transient obtained from the binary gas-phase mixture of benzene and toluene. Again, the same experimental conditions were chosen as in the experiments discussed before. Since each molecule in the mixture irradiates an electromagnetic field, the sum of these fields consists of a coherent sum of the induced polarizations of all components. This opens the possibility to observe beats between modes in the different molecules [24, 29, 98] which are sometimes called polarization beats [99]. The appearance of the signal now is quite different from what is found in the case of pure benzene or toluene samples. From a Fourier analysis we find the vibrational frequencies of toluene, and additionally a frequency which belongs to the energy difference between the modes most strongly excited in benzene and toluene. The theoretical simulation is capable of reproducing the main features of the experimental spectrum, i.e. the strong modulation and the decay behaviour. Nevertheless the agreement is far from perfect. However, the simplified model applied [49] cannot be expected to give better results.

3.5.2 Ground-state vibrational energy flow. As we have seen from the different experiments discussed in this contribution, femtosecond time-resolved FWM is ideally suited for the preparation and probing of ground-state vibrational wave packets. The coherence width of the pump–dump-like ground-state excitation can encompass different vibrational normal modes of a molecule. Therefore, it is possible to study coherent intramolecular vibrational energy redistribution (IVR) in the system under consideration. IVR in isolated polyatomic molecules has been observed in real time before by Felker and Zewail [100–103]. This important process was found in many molecular systems and could be observed by probing the dynamics in time and energy, resolving the phase

change of the different vibrational beats. While these experiments investigated the dynamics in the electronic excited state of molecules, in the following we demonstrate that femtosecond CARS spectroscopy is capable of yielding information about IVR processes taking place in the ground state. While the analysis of the energies and phases of the beats gives the extent of IVR, the decay of the population and beat envelope provides the relaxation times T_1 and T_2, respectively. From this one gains information about the degree of the coupling to bath modes.

The experiments were performed on polymers of diacetylene (PDAs). PDAs exhibit large values of the third-order susceptibility $\chi^{(3)}$ which are comparable to those of inorganic semiconductors [104]. This is due to the fully conjugated backbone structure of the PDA molecules. Figure 20 shows the molecular structure of the diacetylene monomer as well as polymer. The polymers are formed by a topochemical solid-state polymerization [60] and can be described by two resonance forms, the acetylene (left) and the butatriene (right) structure. For a better understanding of the elementary processes in the conjugated system, it is preferable to examine single chains which, owing to their separation, have no marked interaction with each other. Therefore, in some recent work two of us (A.M. and W.K.) studied the properties of polymer chains isolated in single crystals of diacetylene monomers by means of absorption [61, 63, 105], luminescence [61, 105], linear Raman [61, 105–107] as well as nonlinear Raman [61, 105, 108, 109] spectroscopy. These results as well as results from other groups [110, 111] clearly pointed out that the coupling between vibrational modes of the chain and the electronic system of the PDA backbones determines the optical properties of the PDAs. They also show the strong influence of the side-group geometry on the vibronic structure. The dynamics of energy deposition and flow on the ground-state potential-energy surface after optical excitation is of great importance for the complete understanding of these phenomena.

The laser wavelengths for the femtosecond CARS experiment were chosen such that electronic as well as Raman resonances were met. The wavelengths of the two pump lasers were set to $\lambda_{pu_\tau} = \lambda_{pu} = 605$ nm which is close to resonance with the polymer absorption. The Stokes laser had a wavelength of $\lambda_S = 652$ nm in order to excite the vibrational modes in the ground state. These modes are $\tilde{\nu}_2$ (1475 cm^{-1}),
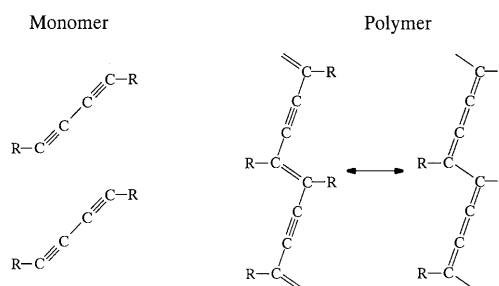
Monomer   Polymer

Fig. 20. The molecular structure of the diacetylene monomer and polymer units. The polymer chain can be described by two mesomeric structures: the acetylenic one (*left-hand side*) and the butatrienic one (*right-hand side*). The experiments discussed in this paper were performed on 'FBS' where R is —CH$_2$—O—SO$_2$—C$_6$H$_4$—F. The backbone of the FBS polymers in the electronic ground state is best described by the acetylenic resonance form while the excited form approaches the butatrienic structure
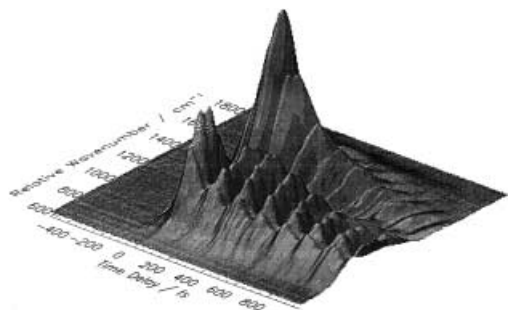
Fig. 21. The correlated time- and wavenumber-resolved CARS signal of polydiacetylene. The observed 3-D pattern was recorded using multichannel detection. For the CARS experiment $\lambda_{pu_\tau} = \lambda_{pu} = 605$ nm and $\lambda_S = 652$ nm were chosen to have both electronic resonance as well as Raman resonance with several backbone vibrational modes

$\tilde{\nu}_{2'}$ (1460 cm^{-1}), $\tilde{\nu}_3$ (1200 cm^{-1}), and $\tilde{\nu}_4$ (960 cm^{-1}) which involve C=C and C−C stretching and bending motions. The mode $\tilde{\nu}_{2'}$ is a side-group CH$_3$ scissors vibration which is coupled to the $\tilde{\nu}_2$ mode by a Fermi resonance.

Figure 21 shows the three-dimensional pattern observed by means of multichannel detection of the anti-Stokes signal (CARS intensity as function of relative wavenumber of the CARS signal and delay time between (pu, S) and pu_τ). The coherence of the wave packet is persistent for times considerably longer than 1 ps. The oscillatory modulation of the CARS transient describes the selective beat pattern and the phases of the different motions. It can be clearly recognized from the 3-D plot that these different dynamics are well separated in wavenumber, which emphasizes the importance to spectrally analyse the nonlinear FWM response.
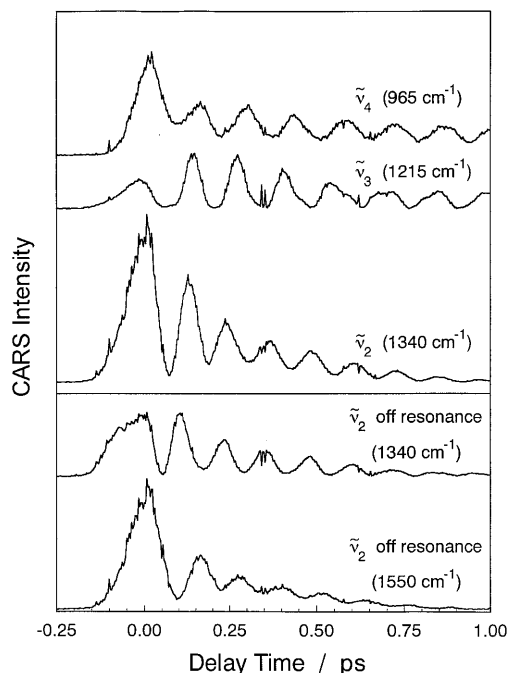
In Fig. 22 different cuts in the 3-D pattern of Fig. 21 are displayed in order to specifically select wavenumber positions corresponding to Raman resonances with the $\tilde{\nu}_2$, $\tilde{\nu}_3$, and $\tilde{\nu}_4$ modes and some in-between values, depicted as 'off-resonance' detection (compare also Fig. 23, where the Raman spectrum as well as the atomic displacement for each considered normal mode is shown). The modulations can be assigned to beatings among the different modes. The interference between $\tilde{\nu}_4$ and $\tilde{\nu}_3$ (240 cm^{-1} difference) is observed in the beating pattern detected at the $\tilde{\nu}_4$ (960 cm^{-1}) wavenumber. For the $\tilde{\nu}_3$ detection (1200 cm^{-1}) the same beating wavenumber is found together with a broad 260–275 cm^{-1} difference, corresponding to $\tilde{\nu}_3 - \tilde{\nu}_2/\tilde{\nu}_{2'}$. Detecting at the wavenumber positions of $\tilde{\nu}_2/\tilde{\nu}_{2'}$ (1475/1460 cm^{-1}) results in beats at 275 and 260 cm^{-1}, respectively. These are the difference wavenumbers of $\tilde{\nu}_3$ with $\tilde{\nu}_2$ and $\tilde{\nu}_{2'}$. The Fermi-resonant modes $\tilde{\nu}_2$ and $\tilde{\nu}_{2'}$ contribute a beat at approximately 15 cm^{-1}.

The beating structures give the interference between different modes which were prepared in-phase by the pump–dump-like interaction of pu and S with the molecules. The resulting modulation periods reflect the wavenumber differences $\tilde{\nu}_i - \tilde{\nu}_j$. Of special interest are the phases of these beatings. Careful examination indicates the sensitivity of the phase change to the detection, on-resonance with a given mode and off-resonance to them. The phase shifts give information about the degree of coupling and the level structure [100–103].

In Fig. 23 the absorption spectrum of the monomer single crystal containing less than 1% PDA molecules is also shown. Polymer and monomer absorption are at clearly different spectral positions. In our experiment the lasers were
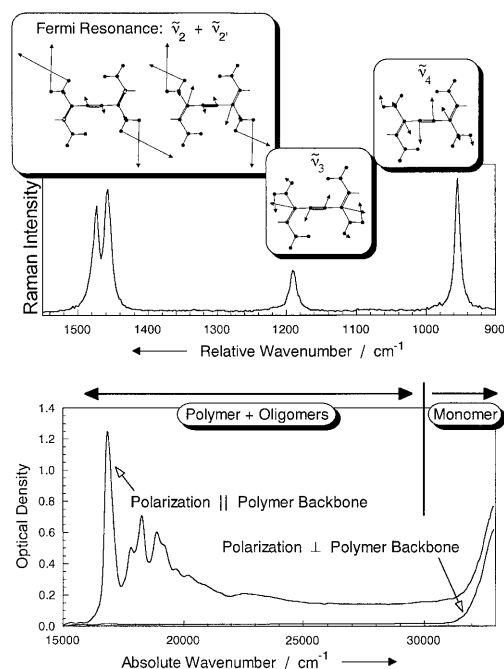

Fig. 22. The temporal behaviour observed for different detection channels (anti-Stokes wavenumbers). This figure represents different cuts made from the 3-D image shown in Fig. 21. Note the phase shifts and in particular those observed for off-resonance cuts (*lower part*)

Fig. 23. *Upper part*: Resonance Raman spectrum displaying the vibrational modes excited by the femtosecond pump and Stokes pulses. For each principal Raman vibrational mode ($\tilde{\nu}_3$, $\tilde{\nu}_4$) as well as for the Fermi-coupled vibrational modes ($\tilde{\nu}_2$, $\tilde{\nu}_{2'}$) atomic displacements are given assuming a simplified side-group structure [113]. *Lower part*: Polarized absorption spectra taken from a single crystal showing polymer and monomer absorption. All spectra were taken at ≈ 10 K

resonant with the absorption of the polymer. Therefore, in the excited state a strong coupling of the excited π electrons along the polymer backbone and the vibrational chain modes takes place as can be seen from the resonance Raman spectrum shown in the same figure. Here, only the backbone modes (except the $\tilde{\nu}_{2'}$ mode which is coupled to $\tilde{\nu}_2$ by Fermi resonance) are enhanced. The electronic transition is connected with a conformational change of the polymer between two mesomeric structures (compare Fig. 20). In the ground state the preferred mesomeric configuration is the acetylenic one, while in the excited state (free-exciton state) the configuration is close to a butatrienic one [112]. Therefore, the ground-state wave packets coherently excited by the resonance CARS process also involve mainly backbone deformations and are determined by the dynamics of these modes.

The PDAs are embedded in a monomer matrix which acts as a bath for the energy deposited in the polymer structure. The resulting relaxation of the modes to the bath can be seen from the decay of the femtosecond CARS signal. Both the population decay (T_1) and the decline of the oscillation amplitudes T_2 can be drawn from the experimental data. For this purpose we use the model given in [10]:

$$S(t) = A\,\mathrm{e}^{-t/T_1} + \mathrm{e}^{-t/T_2} \sum_{i \neq j} C_{ij} \cos(2\pi c \tilde{\nu}_{ij} t + \phi_{ij}). \qquad (3)$$

Here, S is the time-dependent signal, T_1 is the population-decay time, T_2 is the dephasing time, $\tilde{\nu}_{ij} = \tilde{\nu}_i - \tilde{\nu}_j$ is the wavenumber difference between two components and ϕ_{ij} the
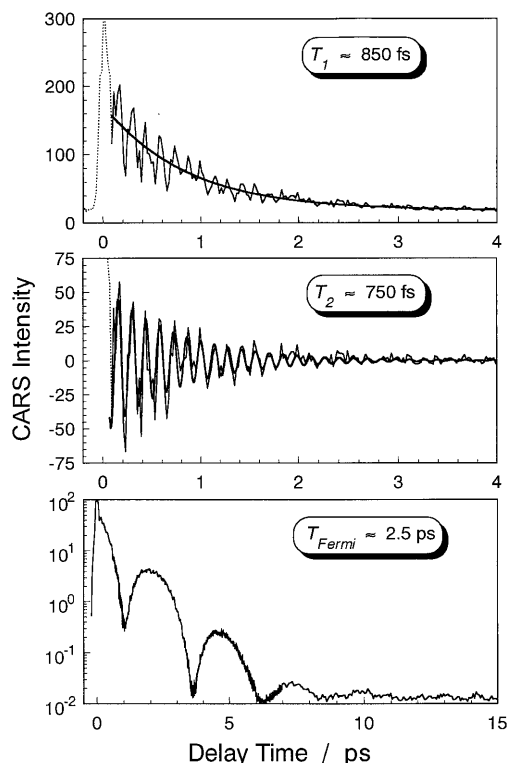
Fig. 24. Experimental and theoretical analysis of coherence, dephasing, and Fermi resonance. In the upper two panels we fit the temporal decay of the signal for the $\tilde{\nu}_4$ mode to the model of [10]. The decay times T_1 and T_2 were obtained accordingly (see text). The *lower panel* shows the long-time behaviour of the $\tilde{\nu}_2$ ($\tilde{\nu}_{2'}$) signal, showing the slow modulation by the Fermi resonance

phase. Some typical results are shown in Fig. 24 for the $\tilde{\nu}_4$ detection. The population-decay time T_1 is ≈ 850 fs and the dephasing time T_2 is of the same order of magnitude, being ≈ 750 fs. The total dephasing rate is the sum of the rates $1/T_1$ and $1/T_2$ [10]. In the same figure we also display the long-time behaviour for $\tilde{\nu}_2$ on a logarithmic scale. The Fermi resonance between $\tilde{\nu}_2$ and $\tilde{\nu}_{2'}$ results in a beating period of ≈ 2.5 ps. These results indicate that the dephasing of the wave packet due to the coupling to the bath modes is slow enough for us to observe the intramolecular vibrational coherence. The coherence time of the nuclear motion is much shorter than the dephasing time and the population-relaxation time.

4 Conclusion

In this paper, we have reviewed our work on femtosecond time-resolved FWM spectroscopy. We concentrated on experimental details. Some of the theoretical work is presented in another contribution to this special issue by Meyer et al. [57].

First, we have demonstrated how the many degrees of freedom the FWM techniques offer, can be used to gain information about molecular wave packet dynamics evolving on different PESs. These experiments were performed on iodine in the gas phase which serves as a simple model system. For the FWM process three lasers interact with the molecules generating a nonlinear response signal. The FWM has to obey energy conservation as well as phase-matching conditions. The coherent signal is well separated from the lasers as a BOXCARS arrangement is used in the experiments. The following parameters are varied: (i) the timing of the laser pulses – using femtosecond laser pulses, we were able to coherently excite and probe wave packets. By changing the sequence of the laser pulses, dynamics on different PESs contribute to the FWM signal. A separation of excited-state and ground-state ro-vibrational coherences is possible and ground-state dynamics can be started and probed even on high vibrational states; (ii) the polarizations of the laser pulses – by changing the polarizations of the laser pulses we were able to suppress the contributions of the rotational motion of the molecules to the FWM signal. This is achieved by a magic-angle geometry; (iii) the laser wavelengths – electronic as well as ro-vibrational resonances and through this the energy position where the wave packets are prepared on the PES of the molecules depend on the laser wavelengths. The ratio of laser wavelengths also determine which FWM process takes place (CARS, DFWM, or CSRS); (iv) the wavelength window which is opened for the detection of the FWM signal – we showed that this parameter is very important as it selects different dynamics contained in the transients. By using a multichannel detection technique 'three-dimensional' transients can be taken which give the FWM intensity as a function of delay time between the laser pulses and wavelength of the FWM signal.

After discussing the possibilities of the femtosecond time-resolved FWM technique, we introduced two specific experiments performed on more-complex molecular systems. Here, we demonstrated that FWM is a very useful method for exciting and probing molecular dynamics in the electronic ground state. That this can be done without any detailed knowledge about the electronic excited PES is shown for ben-

316

zene, toluene, and a binary mixture of benzene and toluene in the gas phase. Here, femtosecond CARS spectroscopy is performed without electronic resonance. The lasers are tuned to coherently excite ground-state vibrational modes around $1000\,cm^{-1}$ in the molecules (Raman resonance). Beating structures are observed from wave packet motion as well as from beats between modes in the different molecules (polarization beats). Relaxation due to rotational dynamics results in a decreasing transient CARS signal. In the other example we applied fs time-resolved CARS to polymers of diacetylene (PDAs) which are embedded in a matrix formed by a single crystal of monomer molecules. These matrix-isolated PDAs offer an interesting system due to their extended delocalized π electrons along the polymer backbone. Here, the CARS process is performed in electronic resonance. The Raman resonance excites several ground-state normal vibrations of the backbone due to the strong coupling of the electronic and vibrational modes. A side-group vibration which is coupled to a backbone vibration by a Fermi resonance also contributes to the dynamics seen from the CARS signal. By spectrally resolving the transient CARS signal we found different beatings between the excited modes. Detecting on-resonance with a specific mode or off-resonance yields phase changes which give information about the IVR in the molecules. An evaluation of the decay of the time-dependent nonlinear response of the system also allowed us to determine the population decay time T_1 and the phase relaxation time T_2. These are found to be considerably longer than the coherence time of the nuclear motion.

The research on the femtosecond time-resolved FWM spectroscopy is continued in our group as well as in other groups. We are convinced that this technique offers a wide field of applications especially when information about ground-state dynamics is needed.

References

1. *Femtosecond Chemistry*, ed. by J. Manz, L. Wöste (VCH, Weinheim, 1995)
2. *Femtochemistry*, ed. by M. Chergui (World Scientific, Singapore 1996)
3. A.H. Zewail: J. Phys. Chem. **97**, 12 427 (1993)
4. A.H. Zewail: *Femtochemistry: Ultrafast Dynamics of the Chemical Bond*, Vols. I+II (World Scientific, Singapore 1994),
5. *Ultrashort Laser Pulses*, *Topics in Applied Physics*, ed. by W. Kaiser (Springer, Berlin 1988)
6. W. Zinth, R. Leonhardt, W. Holzapfel, W. Kaiser: IEEE J. Quantum Electron. **QE-24**, 455 (1988)
7. J. Shah: In *Ultrafast Spectroscopy of Semiconductors and Semiconductor Nanostructures*, Vol. 115 of *Springer Series in Solid-State Sciences*, ed. by M. Cardona (Springer, Berlin 1996)
8. C. Lienau, A.H. Zewail: J. Phys. Chem. **100**, 18 629 (1996)
9. A. Materny, C. Lienau, A.H. Zewail: J. Phys. Chem. **100**, 18 650 (1996)
10. Q. Liu, C. Wan, A.H. Zewail: J. Phys. Chem. **100**, 18 666 (1996)
11. G. Knopp, M. Schmitt, A. Materny, W. Kiefer: J. Phys. Chem. **101**, 4852 (1997)
12. P. Cong, A. Mokhtari, A.H. Zewail: Chem. Phys. Lett. **172**, 109 (1990)
13. T. Baumert, B. Bühler, M. Grosser, V. Weiss, G. Gerber: J. Phys. Chem. **95**, 8103 (1991)
14. T. Lang, K.-L. Kompa, M. Motzkus: Chem. Phys. Lett. **310**, 65 (1999)
15. T. Baumert, V. Engel, C. Meier, G. Gerber: Chem. Phys. Lett. **200**, 488 (1992)
16. T. Baumert, R. Thalweiser, G. Gerber: Chem. Phys. Lett. **209**, 29 (1993)
17. E. Schreiber: In *Proceedings of the International Conference on Lasers'94*, ed. by V.J. Corcoran, T.A. Goldman (STS Press, McLean 1995) p. 490
18. R. de Vivie-Riedle, J. Manz, W. Meyer, B. Reischl, S. Rutz, E. Schreiber, L. Wöste: J. Phys. Chem. **100**, 7789 (1996)
19. C.J. Bardeen, Q. Wang, C.V. Shank: In *Ultrafast Phenomena X*, ed. by P.F. Barbara, J.G. Fujimoto, W.H. Knox, W. Zinth (Springer, Berlin 1996) p. 203
20. T. Lian, S.E. Bromberg, H. Yang, M. Asplund, R.G. Bergman, C.B. Harris, in *Ultrafast Phenomena X*, ed. by P.F. Barbara, J.G. Fujimoto, W.H. Knox, W. Zinth (Springer, Berlin 1996) p. 237
21. P. Anfinrud, R. de Vivie-Riedle, V. Engel: Proc. Natl. Acad. Sci. USA **96**, 8328 (1999)
22. S. Wolf, G. Sommerer, S. Rutz, E. Schreiber, T. Leisner, L. Wöste, R.S. Berry: Phys. Rev. Lett. **200**, 488 (1995)
23. R. Pausch, M. Heid, T. Chen, W. Kiefer, H. Schwoerer: J. Chem. Phys.**110**, 9560 (1999)
24. R. Leonhardt, W. Holzapfel, W. Zinth, W. Kaiser: Chem. Phys. Lett. **133**, 373 (1987)
25. W.E. Bron, T. Juhasz, S. Mehta: Phys. Rev. Lett. **62**, 1655 (1989)
26. M.F.A.A. Laubereau: J. Raman Spectrosc. **21**, 857 (1990)
27. H. Okamoto, K. Yoshihara: J. Opt. Soc. Am. B **7**, 1702 (1990)
28. H. Okamoto, K. Yoshihara: Chem. Phys. Lett. **177**, 568 (1991)
29. T. Joo, M.A. Dugan, A.C. Albrecht: Chem. Phys. Lett. **177**, 4 (1991)
30. M. Fickenscher, H.-G. Purucker, A. Laubereau: Chem. Phys. Lett. **191**, 182 (1992)
31. H. Okamoto, R. Inaba, K. Yoshihara, M. Tasumi: Chem. Phys. Lett. **202**, 161 (1993)
32. T.-S. Yang, R. Zhang, A.B. Myers: J. Chem. Phys. **100**, 8573 (1994)
33. C.C. Hayden, D.W. Chandler: J. Chem. Phys. **103**, 10465 (1995)
34. A. Laubereau, W. Kaiser: Rev. Mod. Phys. **50**, 607 (1978)
35. I.I. Abram, R.M. Hochstrasser, J.E. Kohl, M.G. Semack, D. White: J. Chem. Phys. **71**, 153 (1979)
36. B.H. Hesp, D.A. Wiersma: Chem. Phys. Lett. **75**, 423 (1980)
37. D.D. Dlott, C.L. Schlosser, E.L. Chronister: Chem. Phys. Lett. **30**, 986 (1982)
38. F. Ho, W.S. Tsay, J. Trout, R.M. Hochstrasser: Chem. Phys. Lett. **83**, 5 (1981)
39. W. Zinth, W. Kaiser: In *Ultrafast Laser Pulses and Applications*, ed. by W. Kaiser (Springer, Berlin 1988) p. 235
40. R. Inaba, H. Okamoto, K. Yoshihara, M. Tasumi: Chem. Phys. Lett. **185**, 56 (1991)
41. H.-G. Purucker, V. Tunkin, A. Laubereau: J. Raman Spectrosc. **24**, 453 (1993)
42. T. Joo, A.C. Albrecht: Chem. Phys. **176**, 233 (1993)
43. M. Motzkus, S. Pedersen, A.H. Zewail: J. Phys. Chem. **100**, 5620 (1996)
44. M. Schmitt, G. Knopp, A. Materny, W. Kiefer: Chem. Phys. Lett. **270**, 9 (1997)
45. M. Schmitt, G. Knopp, A. Materny, W. Kiefer: Chem. Phys. Lett. **280**, 339 (1997)
46. S. Meyer, M. Schmitt, A. Materny, W. Kiefer, V. Engel: Chem. Phys. Lett. **281**, 332 (1997)
47. S. Meyer, M. Schmitt, A. Materny, W. Kiefer, V. Engel: Chem. Phys. Lett. **E287**, 753 (1998)
48. M. Schmitt, G. Knopp, A. Materny, W. Kiefer: J. Phys. Chem. A **102**, 4059 (1998)
49. O. Rubner, M. Schmitt, G. Knopp, A. Materny, W. Kiefer, V. Engel: J. Phys. Chem. **A102**, 9734 (1998)
50. T. Chen, V. Engel, M. Heid, W. Kiefer, G. Knopp, A. Materny, S. Meyer, R. Pausch, M. Schmitt, H. Schwoerer, T. Siebert: Vib. Spectrosc. **19**, 23 (1999)
51. T. Chen, H. Dietz, V. Engel, M. Heid, W. Kiefer, G. Knopp, A. Materny, S. Meyer, R. Pausch, M. Schmitt, H. Schwoerer, T. Siebert: SPIE Proc. **3733**, 2 (1999)
52. T. Chen, V. Engel, M. Heid, W. Kiefer, G. Knopp, A. Materny, S. Meyer, R. Pausch, M. Schmitt, H. Schwoerer, T. Siebert: J. Molec. Struct. **480**-**481**, 33 (1999)

53. S. Meyer, M. Schmitt, A. Materny, W. Kiefer, V. Engel: Chem. Phys. Lett. **301**, 248 (1999)
54. T. Siebert, M. Schmitt, T. Michelis, A. Materny, W. Kiefer: J. Raman Spectrosc. **30**, 807 (1999)
55. T. Siebert, M. Schmitt, A. Vierheilig, G. Flachenecker, A. Materny, W. Kiefer: J. Raman Spectrosc. **31**, 25 (2000)
56. A. Vierheilig, T. Chen, P. Waltner, W. Kiefer, A. Materny, A.H. Zewail: Chem. Phys. Lett. **312**, 349 (1999)
57. S. Meyer, V. Engel: Appl. Phys. B **71**, 293 (2000)
58. S. Maeda, T. Kamisuki, Y. Adachi: In *Advances in Non-Linear Spectroscopy*, ed. by R.J.H. Clark, R.E. Hester (J. Wiley & Sons, Chichester 1988) p. 253
59. *Handbook of Chemistry and Physics*, 61st edn, ed. by R.C. Weast, M.J. Astle (CRC Press, Boca Raton 1981)
60. G. Wegner: Z. Naturforsch. **24B**, 824 (1969)
61. A. Materny, W. Kiefer: Macromol. **25**, 5074 (1992)
62. R. Warta, H. Sixl: J. Chem. Phys. **88**, 95 (1988)
63. A. Materny, W. Kiefer: Phys. Rev. B **46**, 2704 (1992)
64. W. Kiefer, H.J. Bernstein: J. Mol. Spectrosc. **43**, 366 (1972)
65. H.A. Ferwerda, J. Terspsta, D.A. Wiersma: J. Chem. Phys. **91**, 3296 (1989)
66. A.B. Myers, R.M. Hochstrasser: J. Chem. Phys. **85**, 6301 (1986)
67. P.M. Felker, A.H. Zewail: J. Chem. Phys. **86**, 2460 (1987)
68. P.M. Felker, A.H. Zewail: Adv. Chem. Phys. **70**, 265 (1988)
69. V. Engel, H. Metiu: J. Opt. Soc. Am. B **7**, 1709 (1990)
70. G.V. Hartland, L.L. Connell, P.M. Felker: J. Chem. Phys. **94**, 7649 (1991)
71. G.V. Hartland, P.W. Joireman, L.L. Connell, P.M. Felker: J. Chem. Phys. **96**, 179 (1992)
72. M. Gruebele, A.H. Zewail: J. Chem. Phys. **98**, 883 (1993)
73. M. Dantus, R.M. Bowman, A.H. Zewail: Nature **343**, 737 (1990)
74. J. Tellinghuisen: J. Chem. Phys. **58**, 2821 (1973)
75. R.F. Barrow, K.K. Yee: J. Chem. Soc. Faraday Trans. II **69**, 684 (1973)
76. J.A. Coxon: J. Quant. Spectrosc. Radiat. Transfer **11**, 443 (1971)
77. J.I. Steinfeld, J.D. Campbell, N.A. Weiss: J. Mol. Spectrosc. **29**, 204 (1969)
78. F. Shimizu, K. Shimizu, H. Takuma: Phys. Rev. A **31**, 3132 (1985)
79. M. Becker, U. Gaubatz, K. Bergmann: J. Chem. Phys. **87**, 5064 (1987)
80. G. Knopp, I. Pinkas, Y. Prior: J. Raman Spectrosc. **31**, 51 (2000)
81. V.V. Lozovoy, B.I. Grimberg, E.J. Brown, I. Pastirk, M. Dantus: J. Raman Spectrosc. **31**, 41 (2000)
82. L. Weiliang, H.-G. Purucker, A. Laubereau: Opt. Commun. **94**, 300 (1992)
83. J. Michl, E.W. Thulstrup: *Spectroscopy with Polarized Light* (VCH, Weinheim 1986)
84. G.R. Fleming: *Chemical Applications of Ultrafast Spectroscopy* (Oxford University Press, New York 1986)
85. R.M. Bowman, M. Dantus, A.H. Zewail: Chem. Phys. Lett. **161**, 297 (1989)
86. S. Gerstenkorn, P. Luc: J. Phys. (Paris) **46**, 867 (1985)
87. M.J. Rosker, M. Dantus, A.H. Zewail: J. Chem. Phys. **89**, 6113 (1988)
88. R.W. Terhune: Solid State Design **4**, 38 (1963)
89. P.D. Maker, R.W. Terhune: Phys. Rev. A **137**, 801 (1965)
90. *Nonlinear Optics of Free Atoms and Molecules*, Vol. 17 of *Springer Series in Optical Sciences*, ed. by D.C. Hanna, M.A. Yuratich, D. Cotter (Springer, Berlin 1979)
91. G.L. Eesley: *Coherent Raman Spectroscopy* (Pergamon Press, Oxford 1981)
92. *Non-Linear Raman Spectroscopy and its Chemical Applications*, ed. by W. Kiefer, D.A. Long (Reidel, Dordrecht 1982)
93. S. Mukamel: *Principles of Nonlinear Optical Spectroscopy*, Vol. 6 of *Oxford Series in Optical and Imaging Sciences* (Oxford University Press, New York, 1995)
94. D. Lee, A.C. Albrecht: In *Advances in Infrared and Raman Spectroscopy*, Vol. 12, ed. by R.J.H. Clark, R.E. Hester (J. Wiley & Sons, Chichester 1985) p. 179
95. D. Lee, A.C. Albrecht: In *Adv. Chem. Phys.*, Vol. 83, ed. by I. Prigogine, S.A. Rice (J. Wiley & Sons, Chichester 1993) p. 43
96. S. Meyer: PhD thesis, Universität Würzburg (1999)
97. F.A. Miller: J. Raman Spectrosc. **19**, 219 (1988)
98. R. Leonhardt, W. Holzapfel, W. Zinth, W. Kaiser: Revue Phys. Appl. **22**, 1735 (1987)
99. L.Q. Lambert, A. Compaan, I.D. Abella: Phys. Rev. A **4**, 2022 (1971)
100. P.M. Felker, A.H. Zewail: J. Chem. Phys. **75**, 5985 (1981)
101. P.M. Felker, A.H. Zewail: Phys. Rev. Lett. **53**, 501 (1984)
102. P.M. Felker, A.H. Zewail: J. Chem. Phys. **82**, 2961 (1985)
103. P.M. Felker, A.H. Zewail: In *Jet Spectroscopy and Molecular Dynamics*, ed. by M. Hollas, D. Phillips (Chapman & Hall, Oxford, 1995) p. 222
104. G.J. Blanchard, J.P. Heritage: J. Chem. Phys. **93**, 4377 (1990)
105. A. Materny, W. Kiefer, M. Schwoerer: J. Chem. Phys. **97**, 2237 (1992)
106. M. Ganz, W. Kiefer, A. Materny, P. Vogt: J. Molec. Struct. **266**, 155 (1992)
107. A. Materny, W. Kiefer: J. Chem. Phys. **97**, 841 (1992)
108. A. Materny, M. Leuchs, T. Michelis, K. Schaschek, W. Kiefer: J. Raman Spectrosc. **23**, 99 (1992)
109. A. Materny, W. Kiefer: J. Raman Spectrosc. **23**, 595 (1992)
110. A.F. Drake, P. Udvarhelyi, D.J. Ando, D. Bloor, J.S. Obhi, S. Mann: Polymer **30**, 1063 (1989)
111. H. Eckhardt, D.S. Boudeaux, R.R. Chance: J. Chem. Phys. **85**, 4116 (1986)
112. T. Kobayashi: J. Lumin. **58**, 117 (1994)
113. D.N. Batchelder, D. Bloor: J. Polym. Sci. Polym. Phys. Ed. **17**, 569 (1979)